M. A. SOKOLOVSKIY
Water Problems Institute of the Russian Academy of Sciences, 3, Gubkina Str., 119991, Moscow, GSP-1, Russia
E-mail: sokol@aqua.laser.ru

J. VERRON
Laboratoire des Ecoulements Géophysiques et Industriels, UMR 5519, CNRS, BP53 X, 38041, Grenoble Cedex, France
E-mail: verron@hmg.inpg.fr

DYNAMICS OF TRIANGULAR TWO-LAYER VORTEX STRUCTURES WITH ZERO TOTAL INTENSITY

Received June 28, 2002 DOI: 10.1070/RD2002v007n04ABEH000221

The problem of three vortex lines in a homogeneous layer of an ideal incompressible fluid is generalized to the case of a two-layer liquid with constant density values in each layer. For zero-complex-momentum systems the theory of the *roundabout* two-layer tripole is built. When the momentum is different from zero, based on the phase portraits in trilinear coordinates, a classification of possible relative motions of a system composed of three discrete (or point) vortices is provided. One vortex is situated in the upper layer, and the other two in the lower layer; their total intensity is zero. More specifically, a model of a two-layer tripole is constructed, and existence conditions for stationary solutions are found. These solutions represent a uniform translational motion of the following vortex structures: 1) a stable collinear configuration *triton*, a discrete analog of the vortex structure *modon+rider*, 2) an unstable triangular configuration. Features of the absolute motion of the system of three discrete vortices were studied numerically.

We compared the dynamics of a system of three point vortices with the dynamics of three finite-core vortices (vortex patches). In studying the evolution of the vortex patch system, a two-layer version of the Contour Dynamics Method (CDM) was used. The applicability of discrete-vortex theory to the description of the finite-size vortex behavior is dicussed. Examples of formation of vortical configurations are given. Such configurations appear either after merging of vortices of the same layer or as a result of instability of the two-layer vortex structure.

1. Introduction

The study of discrete vortex interaction in an infinite volume of ideal liquid has been an ongoing hydrodynamics problem for a century and a half [1, 2, 3, 4, 5, 6, 7, 11, 20, 34, 36, 41, 42, 43, 44, 45, 47, 48, 50, 52, 54, 55, 56, 64, 65, 67, 68, 69]. The key problem, the integrability of equations, remains open. In the general case, a system that consists of a large number of vortices is nonintegrable; solutions can be obtained only for some specific cases, e.g. when the initial location of the vortices has some symmetry properties [2, 3, 11, 26, 36, 42, 45, 47, 48, 50]. In [69] Ziglin proved the nonintegrability of the problem of four arbitrarily located vortices (even with the assumption that one of them is of zero strength, i.e. simply a liquid particle); the studies [41, 48] provide a description of the stochastic properties of such a system. Special cases of four-vortex integrability are discussed in [7, 11, 31, 41, 42, 44, 45, 55, 57, 58, 59, 60, 66, 68]. However, the problem with three vortices is always integrable as demonstrated in [1, 11, 36, 45, 50]. The problem has been attracting ongoing interest for some considerable time [1, 4, 11, 27, 34, 42, 43, 45, 47, 50, 54, 55, 56, 64, 65, 67, etc.]. This interest is not

Mathematics Subject Classification 76C05

only related to the vortex problem itself, but also to its numerous analogs in rigid body mechanics, astrophysics, the dynamics of superfluid helium, and the mathematical biology [4, 8, 11, 36, 45]. Further interest to this problem was due to the identification of so-called tripolar structures [39], symmetrical three-vortex formations of the $(-\kappa, 2\kappa, -\kappa)$ type, and the discovery of their existence in chaos [38] (here κ is vortex intensity). These vortex constructions are stable for a sufficiently wide range of external parameters [12]. The study of three-vortex dynamics with non-zero total intensity of the particular $(-\kappa, \kappa, \kappa)$ type was started in [1], and completed in [34, 44, 45]. In the overwhelming majority of the studies [1, 2, 3, 4, 5, 6, 7, 11, 12, 14, 15, 17, 20, 24, 27, 28, 29, 30, 34, 36, 37, 38, 39, 40, 42, 43, 44, 45, 46, 47, 48, 49, 50, 51, 52, 53, 54, 55, 56, 63, 64, 65, 67, 69] the problems of vortex dynamics are investigated within the framework of the homogeneous fluid model. In geophysical problems density stratification is crucial (the reader is referred to [9, 10, 16, 18, 19, 22, 23, 25, 26, 28, 31, 33, 35, 57, 58, 59, 60, 61, 62, 68]). In particular tripolar structures are observed not only in homogeneous fluids [12, 14, 27, 29, 30, 37, 38, 40, 49, 51, 53, 67], but also in stratified fluids [9, 10, 13, 16, 18, 19, 22, 28, 33, 57, 58, 59, 61, 62].

In the present paper we provide a detailed analysis of the problem of three vortices with zero total intensity in a two-layer fluid. Some of these results are summarized in the note [61].

Two approaches — discrete and continuous — are used.

2. Formulation of the problem of three vortices in a two-layer fluid

We adopt the following assumptions: a) the non-dimensional thicknesses of the upper and lower layers are the same ($h_1 = h_2 = 1/2$), and the fluid densities ρ_1 and ρ_2 satisfy the condition $\Delta\rho = \rho_2 - \rho_1 \ll \rho_1 + \rho_2$; b) one vortex is located in the upper layer, and the two others in the lower layer. In this case, the complex form of the equation of motion for the three discrete vortices in two immiscible liquid layers rotating with constant angular velocity (the "solid lid" condition being applied to the upper interface) can be written as

$$\frac{d\overline{z_1^1}}{dt} = \frac{1}{4\pi i}\sum_{j=1}^{2}\frac{\kappa_2^j}{z_1^1 - z_2^j}\Big[1 - \gamma|z_1^1 - z_2^j|K_1\Big(\gamma|z_1^1 - z_2^j|\Big)\Big], \tag{2.1}$$

$$\frac{d\overline{z_2^m}}{dt} = \frac{1}{4\pi i}\Big\{\frac{\kappa_1^1}{z_2^m - z_1^1}\Big[1 - \gamma|z_2^m - z_1^1|K_1\Big(\gamma|z_2^m - z_1^1|\Big)\Big] + \frac{\kappa_2^{3-m}}{z_2^m - z_2^{3-m}}\Big[1 + \gamma|z_2^m - z_2^{3-m}|K_1\Big(\gamma|z_2^m - z_2^{3-m}|\Big)\Big]\Big\}. \tag{2.2}$$

Here $z_n^m = x_n^m + iy_n^m$ is the complex coordinate of the m-th vortex from the n-th layer (the superscript indicates the number of the two-layer vortex, and the subscript the number of the layer: 1 — upper layer, 2 — lower layer); κ_n^m is the intensity of this vortex; the line over z_n^m denotes complex conjugation; the parameter γ is inversely proportional to the internal Rossby deformation radius $\lambda = [g\Delta\rho h_1 h_2/\rho_0 f^2(h_1+h_2)]^{\frac{1}{2}}$; K_k is a modified Bessel function of the k-th order; g is the gravitational acceleration; f is the Coriolis parameter equal to double the angular rotation velocity of the fluid plane around the axis normal to it. This axis and the orthogonal axes x and y form a left coordinate system. According to the second of the above assumptions, the variable m in (2.2) takes values 1 and 2. So equations (2.1)–(2.2) represent a system of three ordinary differential equations, which must be supplemented with initial conditions.

The system of equations (2.1)–(2.2) is hamiltonian with Hamiltonian

$$H = -\frac{1}{4\pi}\Big\{\kappa_2^2\kappa_2^1\Big[\ln d_{22}^{12} - K_0\Big(\gamma d_{22}^{12}\Big)\Big] + \kappa_1^1\kappa_2^1\Big[\ln d_{21}^{11} + K_0\Big(\gamma d_{21}^{11}\Big)\Big] + \kappa_1^1\kappa_2^2\Big[\ln d_{21}^{21} + K_0\Big(\gamma d_{21}^{21}\Big)\Big]\Big\}, \tag{2.3}$$

(where $d_{kl}^{mn} = |z_l^n - z_k^m|$), and can be written in the standard Hamiltonian form. In addition to (2.3), the initial system also has the following integrals:

$$\text{momentum} \quad P = \kappa_1^1 z_1^1 + \kappa_2^1 z_2^1 + \kappa_2^2 z_2^2, \quad \overline{P} = \kappa_1^1\overline{z_1^1} + \kappa_2^1\overline{z_2^1} + \kappa_2^2\overline{z_2^2},$$

$$\text{and angular momenta} \quad M = \kappa_1^1|z_1^1|^2 + \kappa_2^1|z_2^1|^2 + \kappa_2^2|z_2^2|^2.$$

Their numerical values are determined by the initial conditions. It is easy to check that the invariants H, M and $P \cdot \overline{P}$ are in involution, and thus the system (2.1)–(2.2) always has a regular solution [11, 36, 45]. In the following sections we will assume that the total intensity of the vortices is zero, and examine the two special cases

$$I : \kappa_1^1 = -2\kappa, \kappa_2^1 = \kappa_2^2 = \kappa; \tag{2.4}$$

$$II : \kappa_1^1 = \kappa_2^2 = -\kappa, \kappa_2^1 = 2\kappa; \tag{2.5}$$

where $\kappa > 0$. In doing so, we assign anticyclonic vorticity to the upper layer vortex. In case I, it is compensated by two cyclones of equal intensity in the lower layer. In case II the total circulation (that is equal to zero) is ensured by the combination of the intensities of a strong cyclone and half an anticyclone in the lower layer.

Peculiarities of the absolute motion of discrete vortices were studied by solving equations (2.1)–(2.2) numerically using the standard second-order Runge–Kutta method.

We will also examine *vortices of finite size* or *vortex patches* which are closed regions on the plane (x, y) with piecewise-constant values of the potential vorticity Π_i^{j1}. The evolution of vortex patches will be simulated using the two-layer version of the CDM [35]; periodic cubic spline techniques will be used.

The cases $P = 0$ and $P \neq 0$ will be examined in greater detail.

3. Three vortices with zero total momentum

Without loss in generality, initially, we can place the vortex whose intensity differs in sign from the intensities of the other vortices at the origin of coordinates. When $P = 0$, the center of vorticity of the three vortices remains motionless. In the following sections, we study all possible motions of such vortex systems.

3.1. Model of symmetric two-layer tripole

3.1.1. Discrete vortices

Let us assume that condition I is satisfied, i. e. the anticyclonic vortex of the upper layer takes the central position, and the cyclones of the lower layer are at the periphery (Fig. 1a). The triangle indicates the upper-layer vortex, and the circle and the square[2] the positions of the lower-layer vortices.

[1]The value $\Pi_i^j S_i^j$ is an analog of vortex intensity (S_i^j is the area of the j-th vortex patch in the i-th layer). We assume that the equation $\lim_{S_i^j \to 0} \Pi_i^j S_i^j = \kappa_i^j$ is satisfied.

[2]The same notations will also be used in the subsequent figures.

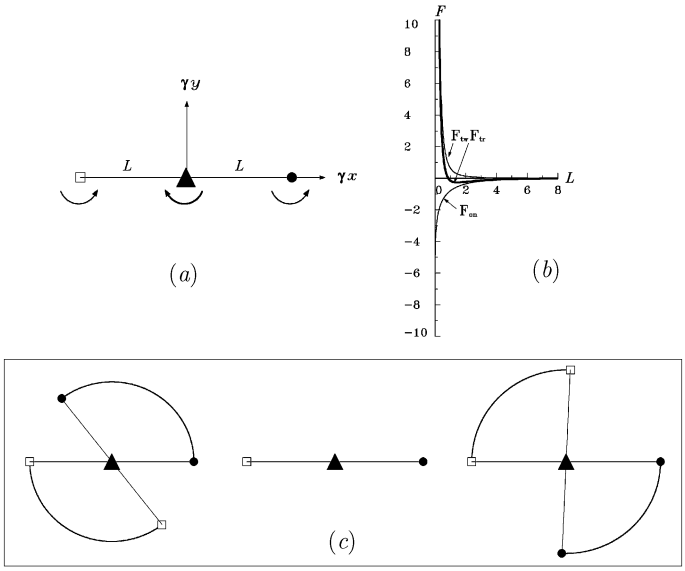

Fig. 1. Characteristics of the tripolar system of the *Ordinary* or *Inverse Roundabout* types:(a) Scheme of the vortex location. Arched arrows indicate the direction of vortex rotation, the thickness being proportional to their intensity; (b) Dependency equations (3.1), (3.3) for the angular velocity of the cyclonic vortex rotation in the lower layer: $F_{tr}(L)$ — thick line, $F_{tw}(L)$ and $F_{on}(L)$ — thin lines; (c) From left to right: trajectories of the vortex motion of the discrete tripolar structure at $L = L_0 - \Delta L$ — inverse roundabout, $L = L_0$ — intermediate stationary state and $L = L_0 + \Delta L$ — ordinary roundabout ($\Delta L = 0.06$ and $L_0 = 0.8602$). Horizontal segments join the initial vortex positions.

The marker size reflects the absolute value of vortex intensity (the triangle, showing the location of the strong upper-layer vortex, is larger than the circle and the square corresponding to the lower-layer cyclones of less intensity). As shown in [64], for the case of homogeneous fluid, we can interpret such a vortex system as a discrete model of a tripolar vortex (in this case, a two-layer vortex). In [59] we referred to a connected vortex configuration, composed of an upper layer core and two satellites located in the lower layer and having opposite cyclonicity, as a *roundabout* by analogy with a funfair ride that has a rotating horizontal disk and seats attached to it from beneath. The seats are able to revolve around their instantaneous axes by swivelling[3].

It is known that the peripheral vortices of a *barotropic* tripolar structure always rotate with constant angular velocity in the direction dictated by the vorticity sign of its core. In the *two-layer* case, the expression for the angular velocity of the motion of the bottom cyclonic vortices with respect to the anticyclonic upper-layer core takes the form

$$\omega = \frac{\kappa\gamma^2}{4\pi L^2}\left\{L\Big[K_1(2L) + 2K_1(L)\Big] - \frac{3}{2}\right\} \equiv \frac{\kappa\gamma^2}{4\pi}F_{tr}\big(L\big), \tag{3.1}$$

where $L = \gamma l$, and l is the distance of the central vortex to each of the peripheral vortices (i. e. their circular-orbit radius). Let us represent the function F_{tr}, which is proportional to the angular velocity of the rotation of the cyclonic vortices in the two-layer tripole, as the sum

$$F_{tr} = F_{tw} + F_{on}, \tag{3.2}$$

[3]Carton and the co-authors [9, 13, 18, 19] have proposed to call such configurations in the more general case, when vortex-satellites do not obviously belong to the same layer, *arch-shaped vortices*. Below this term will be used to refer to an arbitrary structure of one upper-layer vortex and two lower-layer vortices such that $P \neq 0$.

where

$$F_{tw} = \frac{1}{L^2}\Big[LK_1(2L) + \frac{1}{2}\Big], \qquad F_{on} = \frac{2}{L^2}\Big[LK_1(L) - 1\Big]. \tag{3.3}$$

Here F_{tw} is determined by the interaction of the lower-layer cyclonic vortices, and F_{on} by the influence of the upper-layer anticyclone on them.

The following estimations are valid

$$\Big(F_{tr}, F_{tw}, F_{on}\Big) \asymp \begin{cases} \left(\frac{1}{L^2}, \frac{1}{L^2}, \ln\left(\frac{Le^{-\gamma/2}}{2}\right)\right), & L \ll 1, \\ \left(-\frac{3}{2L^2}, \frac{1}{2L^2}, -\frac{2}{L^2}\right), & L \gg 1. \end{cases}$$

In this case $F_{on} < 0$, $F_{tw} > 0$ and $(F_{on})' > 0$, $(F_{tw})' < 0$ for all L, and the function $F_{tr}(L)$ changes its sign at the $L = L_0$ such that

$$K_1(2L) + 2K_1(L) = \frac{3}{2L}, \tag{3.4}$$

and reaches its minimum value at the point L where

$$L\Big[K_0(2L) + K_0(L)\Big] + K_1(2L) + 2K_1(L) = \frac{3}{2L}. \tag{3.5}$$

Approximate solutions of the transcendental equations (3.4) and (3.5) are $L = L_0 = 0.8602$ and $L = L_{min} = 1.4404$, respectively.

Figure 1b shows how the values F_{tr} , F_{tw} and F_{on} depend on L (equations (3.1) and (3.3)). The graphs $F_{tr}(L)$ and $F_{tw}(L)$ show that the most effective interlayer interaction takes place in a vicinity of L_{min}.

Figure 1c displays discrete vortex trajectories for the three cases: $L < L_0$, $L = L_0$ and $L > L_0$. Initially, the three vortices are on a horizontal straight line. In the balance of forces for $L > L_0$ the influence of the anticyclone on the vortices of the lower layer prevails, and the configuration as a whole, is similar to that of a barotropic tripole rotating in an anticyclonic direction. Hereafter, we will refer to such a vortex construction as an *Ordinary Roundabout (OR)*. When L is small, intra-layer interaction plays the main role[4], as clearly shown in Fig. 1b. Therefore, despite the anticyclonic swirl imposed by the upper-layer vortex, the cyclonic lower-layer vortices rotate anticlockwise in circular orbits. Such a configuration will be referred to as an *Inverse Roundabout (IR)*. In the intermediate (unstable) equilibrium configuration ($L = L_0$), all the vortices are at rest.

Thus, a circular rotation of satellite vortices in the two-layer tripole can occur both in the direction induced by the central core, and in the opposite direction due to the interaction between the satellites. Figure 1c also illustrates specific behavior features of $F_{tr}(L)$ when the initial positions of the lower-layer vortices are away from the points with coordinates L_0 and $-L_0$ by $\Delta L > 0$. At $L = L_0 + \Delta L$, the *anticyclonic* trajectories of the lower-layer vortices are represented by quadrant arcs. Each vortex in the lower layer, in the same time span, covered a distance about one and a half times greater in the *cyclonic* direction (at $L = L_0 - \Delta L$). This can be explained by the different behavior of F_{tr} on the intervals $0 < L < L_0$ and $L_0 < L < L_{min}$ (Fig. 1b).

It is important to note that the behavior of the two-layer tripole (in particular, the location of the points where the change of sign of the angular velocity and its derivative occurs) is determined by functions of $L = \gamma l$, i. e. by the ratio of the geometrical vortex-formation size l to the radius of deformation. Within the framework of discrete-vortex theory, the magnitude of the deformation radius affects only the value of the angular velocity of the discrete tripolar structure (see (3.1)). In the dynamics of finite-core (or distributed) vortices, the parameter γ will play the predominant role (this will be discussed in section 3.1.2).

[4]Gryanik [23] was the first to point to this fundamental property of two-layer vorteces interaction.

3.1.2. Finite-core vortices

As mentioned above (see [38]), coherent structures of the finite-core tripole type could arise spontaneously in an arbitrarily distributed vortex field. Among other possible mechanisms involved in their formation, mention may be made of the instability of the vortex which initially is axially symmetric [10, 13, 14, 15, 19, 22, 28, 29, 32, 40, 46, 59, 63] (contrary to the grazing collision of two dipoles [37, 49, 57, 58, 59]) as well as the effect of a submerged hill on a heton [62].

In the case of *finite-core vortices*, in addition to the distance between the vortex centers (analog of l), there is one more geometric parameter, namely, the characteristic radius of the vortex patch r (and, in this case, the combination $R = \gamma r$ occurs). In particular, it is known that merging occurs between close vortex patches and, under certain conditions, they can become unstable and break out into smaller vortex structures. In the section below, numerical results demonstrate these properties of finite-core vortices.

As mentioned above, the calculations for the finite-core vortices were made using the two-layer version of CDM [35]. In most numerical experiments (except those shown in Fig. 5), all three-vortex patches (at the initial moment) formed circles[5] of unit radius (normalized by the Rossby deformation radius). The distribution of the potential vorticity was set to be $\Pi_1^1 = -2\Pi$, $\Pi_2^1 = \Pi_2^2 = \Pi$, where $\Pi > 0$. We chose the value of Π such that one unit of dimensionless time corresponds to the rotational period of a fluid particle belonging to the boundary of a hypothetical cylindrical two-layer vortex-heton with constant values of potential vorticity -2Π and 2Π in the upper and lower layers, respectively. Furthermore, the layer to which the liquid particles belong is of no importance, since the absolute values of azimuth velocities in circular contours of such a compensated vortex coincide.

Figure 2 shows the results of a series of numerical computations performed to study the properties of finite-core two-layer tripoles. This is a diagram in the plane of the parameters (γ, l) for $\gamma \in (0; 3]$, $l \in [1; 3]$ (the minimum value $l = 1$ corresponds to the case when the contours of initially circular vortex patches in the lower layer touch one another). The dashed line in this figure represents the hyperbola $\gamma l = L_0$, which separates the areas OR and IR for the discrete vortices. As seen from the figure, new areas appear for the finite-core vortices: ORM (*Ordinary Roundabout* with *Merging* of the bottom-layer vortex patches), IRM (*Inverse Roundabout* with *Merging* of the bottom-layer vortex patches), as well as UOR (*Unstable Ordinary Roundabout*) and $UORM$ (*Unstable Ordinary Roundabout* after intermediate *Merging* of the bottom-layer vortex patches).

Before presenting the results of computations, we will describe, using Fig. 2, the finite-core vortex behavior:

(1) In contrast to the case of *discrete vortices*, the boundary between the regions IR and OR in the *continuous* case is no longer characterized by the unique constant L_0 because the corresponding curve in Fig. 2 is not a hyperbola.

(2) When $l \geqslant 2$, the theory of discrete vortices is applicable to the finite-core two-layer vortex structures in the part of the external parameters field under examination. Hence, if the centers of initially circular vortex patches in different layers are separated by a distance larger than four radii, the qualitative behavior of the finite-core roundabout is analogous to that of the point vortices.

(3) As $\gamma \to 0$, the lower-layer vortices start merging for $l < 1.6$. This is in agreement with the results obtained for the vortices in a homogeneous fluid [17, 32]. In fact, the limit $\gamma \to 0$ corresponds to the case of a "solid lid" at the interface between the layers. In this case, the anticyclone of the upper layer hadrly affects the dynamics of the lower layer, and the barotropic conditions are fulfilled for the cyclones located in it.

[5] It is obvious that, in the course of vortex patch interaction, vortex contours become deformed, evolving together with liquid particles located within them.

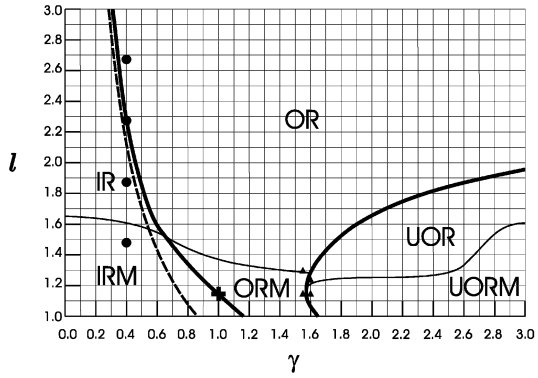

Fig. 2. Diagram of the different states of the two-layer tripolar vortex structures in the plane of parameters (γ, l). Thick lines separate the areas OR, IR and UOR, and thin lines in each of these areas represent boundaries of sub-areas ORM, IRM and $UORM$, where merging of the bottom vortex patches may be observed. A dashed line separates the existence areas for OR and IR (discrete vortices). Marker positions correspond to the parameter γ and l values for the calculations illustrated by Figs. 3, 4 and 27a.

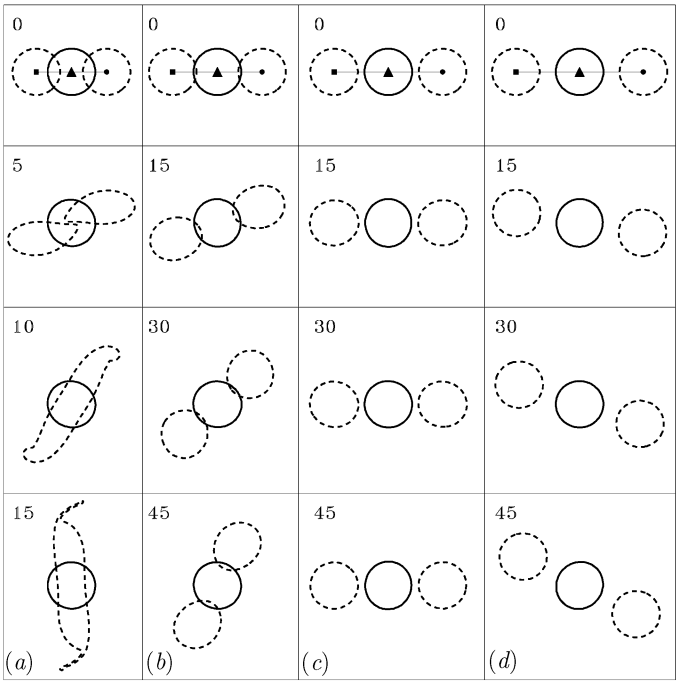

Fig. 3. Two-layer tripolar vortex patch structures where $\gamma = 0.4$ and $l = 1.48$ — (a), $l = 1.88$ — (b), $l = 2.28$ — (c), $l = 2.68$ — (d). In the upper left corner of each frame, the moments of dimensionless time are given. Contours of the upper-layer vortices are plotted with a solid line, and lower-layer vortices with a dashed line. Horizontal segments, linking the vortex centers, represent the collinear character of their initial state. Circular markers in Fig. 2 correspond to the conditions of these numerical experiments.

(4) With γ increasing, merging of the lower-layer cyclones occurs when their centers are initially closer to each other. This means that if the stratification becomes less pronounced, the "pushing aside" effect of the upper-layer core increases. This phenomenon takes place in the regions IR and OR.

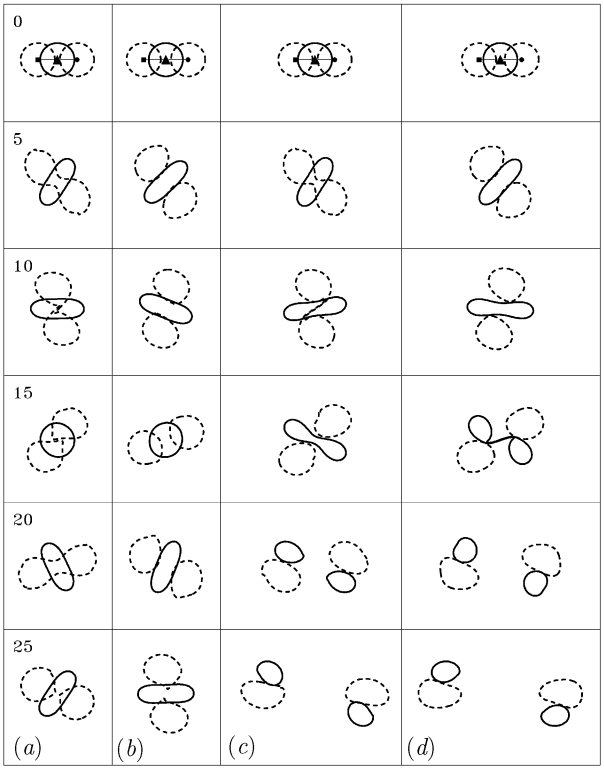

Fig. 4. The same as in Fig. 3, but at $\gamma = 1.55$: $l = 1.15$ — (a), $l = 1.30$ — (b);$\gamma = 1.60$: $l = 1.15$ — (c), $l = 1.25$ — (d). Triangular markers in Fig. 2 correspond to the conditions of these numerical experiments.

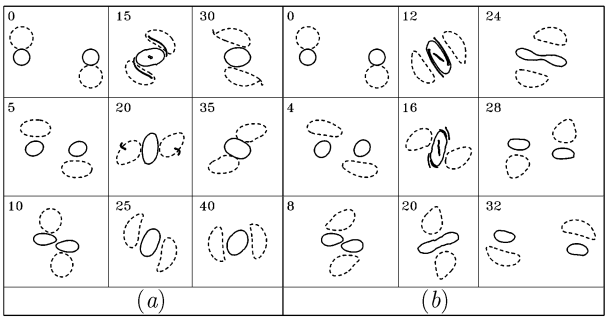

Fig. 5. Non-head-on collision of two hetons with tilted axes, which consist of initially circular vortex patches with centers located at the points $(x_1^1;\, y_1^1) = (-x_1^2;\, y_1^2) = (-3;\, 0)$, $(x_2^1;\, y_2^1) = (-x_2^2;\, -y_2^2) = (-3;\, 1 + 1/\sqrt{2})$: (a) $\gamma = 1.6$ (OR is formed); (b) $\gamma = 2.8$ (UOR is formed).

(5) When $\gamma \geqslant 1.6$, tripolar vortex structures with sufficiently close vortex-patch centers ($l < 2$) could be unstable.

The following figures demonstrate the properties of the finite-core tripoles. There properties are summarized in Fig. 2.

Figure 3 shows vortex-patch configurations for two-layer tripoles with $\gamma = 0.4$ (relatively strong stratification) and for different values of l, the initial distance between the center of the upper-layer vortex and those of the lower-layer vortices located symmetrically on either side of it. The first column (Fig. 3a) demonstrates the realization of the regime IRM, which caused the formation of a two-layer

structure composed of a practically circular upper-layer anticyclone and a quasi-elliptic cyclone in the bottom layer formed by the merging of the same-layer vortex-satellites. As the distance l increases, we observe firstly configurations of the IR type (Fig. 3b), then of the OR type (Fig. 3d). An intermediate (unstable) state with practically motionless vortex patches has been "caught" (see Fig. 3a). During the computation, the movements of the lower-layer vortices (normalized by the value of the deformation radius) are of $O(10^{-2})$. In this case $L = 0.9120$, which differs, of course, from the corresponding value $L = L_0 = 0.8602$ observed in the case of point vortices.

Figure 4 completes the demonstration of the topologically different finite-core vortex configurations:

Figure 4a — ORM. The cyclones of the bottom layer periodically merge and then separate again. In the course of mixing, after splitting, fluid particles initially located inside one of the vortex patches may move to another vortex patch. In doing so, a few lower-layer liquid particles may regularly rotate anticlockwise, but, as a whole, the vortex structure behaves as an ordinary roundabout[6].

Figure 4b — OR. Here, it is possible to see the formation of OR with a small limiting value of l. Unlike the situation in Fig. 3d, on which this type of motion was also observed, the anticyclonic vortex in the upper layer deforms by taking the shape of an elongated oval.

Figure 4c — $UORM$. After a relatively short intermediate stage when the lower-layer vortices merge, separation occurs. Then the anticyclone of the upper layer splits into two parts, resulting in two two-layer vortices with tilted axes running in opposite directions. During the process of filamentation, only a small part of the vortex-patch total surface is lost (approximately 4%). Thus, after their separation, the conditions $\Pi_1^1 S_1^1 + \Pi_2^1 S_2^1 = 0$ and $\Pi_1^2 S_1^2 + \Pi_2^2 S_2^2 = 0$ (S_i^j it is area of the vortex patch with potential vorticity Π_i^j) are satisfied with a sufficient degree of accuracy for each of the two-layer vortices. Therefore, the diverging motion of two-layer vortex structures (hetons) [59] is approximately rectilinear.

Figure 4d — UOR. Splitting into two diverging hetons with tilted axes occurs with no intermediate stage of lower-layer vortices merging. Because of this, the decay of the upper-layer vortex occurs more rapidly than in the previous case; and the two-layer pairs diverge over a greater distance in the same time interval as in Fig. 4c.

Remark 1. The experiments represented in Figs. 4a and 4c were carried out with one and the same value of l and very close values of γ. Nevertheless, they provide examples of different types of motion because in these experiments the points of the plane (γ, l) lie in the different regions, namely, in ORM and $UORM$ (the two triangular markers in lower part of Fig. 2).

Remark 2. It is possible to "reverse" the process of the splitting of the unstable tripole into two scattering hetons (Figs. 4c, 4d) by exchanging the locations of the vortex patches in each of the two-layer pairs in such a way that their initial disposition could promote the initialization of the grazing process. Two examples of the formation of two-layer tripolar structures caused by such collisions are shown Fig. 5. Here, we choose the initial parameters in such a way as to be close to the case discussed above. In both cases, a two-layer tripolar structure arises at $l \approx 1.8$, but when $\gamma = 1.6$ (Fig. 5a), it is stable, and when $\gamma = 2.8$ (Fig. 5b), it is unstable, as summarized in Fig. 2. The experiment shown in Fig. 5b can be interpreted as an example of inelastic collision of two hetons proceeded by their reverse motion; this is accompanied by a sign change of the axis slope angle, and the upper-layer vortex patches lose their individual properties (during the merging stage).

3.2. Model of an Eccentric Roundabout

3.2.1. Discrete vortices

Let $\binom{i}{j}$ stand for the i-th vortex of j-th layer, and let condition II now be satisfied, the strongest lower-layer cyclonic vortex $\binom{1}{2}$ is centrally positioned at the origin of coordinates, and the anticyclones $\binom{1}{1}$ and $\binom{2}{2}$ are at a distance $l = L/\gamma$ from the cyclonic vortex, i. e. $P = 0$. In this case,

[6]The segregation criterion for areas IRM and ORM in Fig. 2 was the definition of the direction of rotation of the cyclonic vortex centers before they merged.

peripheral vortices belong to different layers and, despite the geometric symmetry, their interaction with the cyclone is governed by different laws. Because of momentum invariance, in these conditions, the distance between the vortices remains constant. The vortex system must rotate as a whole around the vorticity center. Unlike the previous case, this center does not lie at the origin of coordinates.

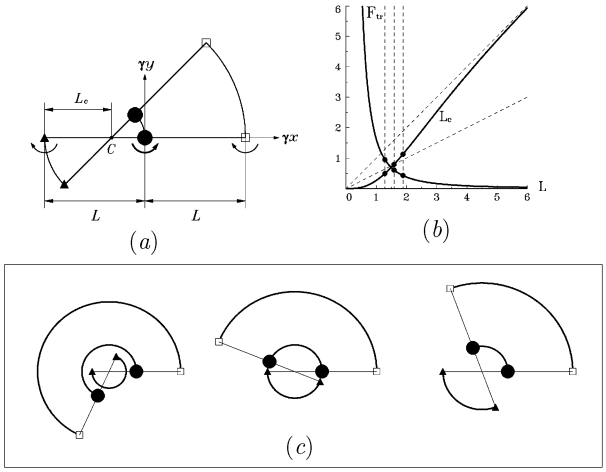

Fig. 6. Characteristics of the tripolar structure of the *Eccentric Roundabout* type: (a) Scheme of the dislocation and motion of the vortices. The point C marks the vorticity center; (b) Dependency equations (3.8)–(3.9) as functions of L. Points in the curves correspond to the parameter values used in the calculations for Fig. 6c; Inclined dashed lines present the functions $L_c = L$ and $L_c = 2L$. (c) From left to right: trajectories of the vortex motion at $L_c < L/2$, $L_c = L/2$ and $L_c > L/2$ and, respectively, $L = 1.29$, $L = 1.59$ and $L = 1.89$. Linear segments link the locations of the three vortices in the initial and final (calculated) moments.

Let V_i^j be the azimuth velocity of the vortex $\binom{j}{i}$. Then, according to the equation of motion (2.1)-(2.2), for the vortices $\binom{1}{1}$ and $\binom{1}{2}$ to rotate around the point C (Fig. 6a) with angular velocity ω the following must hold

$$\frac{|\omega|}{\gamma} = \frac{|V_1^1|}{L_c} = \frac{|V_2^1|}{L - L_c}. \tag{3.6}$$

By virtue of momentum conservation, the system of the three vortices rotates as a solid body around the vorticity center C with coordinates

$$(L_c - L; 0) \tag{3.7}$$

with respect to the coordinates $(\gamma x, \gamma y)$. For a fixed value of L, from (3.6)–(3.7) we obtain

$$\omega = \frac{\kappa\gamma^2}{4\pi L^2}\Big(LK_1(2L) + \frac{3}{2}\Big) \equiv \frac{\kappa\gamma^2}{4\pi} F_{tr}(L) \tag{3.8}$$

(compare with (3.1))

$$L_c = L - \frac{2K_1(L)}{F_{tr}(L)}. \tag{3.9}$$

It is easy to obtain asymptotic estimations from (3.8)–(3.9)

$$\left(L_c, F_{tr}\right) \asymp \begin{cases} \left(\dfrac{L^2 ln2}{2}, \dfrac{2}{L^2}\right), & L \ll 1, \\ \left(L, \dfrac{3}{2L^2}\right), & L \gg 1. \end{cases}$$

The L-dependence of these variables is shown in Fig. 6b. Thus, the system composed of three collinear vortices rotates around the vorticity center in the cyclonic direction due to the stronger vortex of the bottom layer. This system is formed in such a way that the upper-layer vortex is always located at one side of the vorticity center, and the two lower-layer vortices are at the other side. In this case, the vortex structure resembles a two-level *Eccentric Roundabout* rotating anticlockwise. Moreover, the lower-layer "chair" placed closer to the vorticity center, also revolves around its own axis anticlockwise, and two peripheral "chairs" (one in the upper level and the other in the lower) rotate at half this speed in the opposite direction. For small (large) values of L, the inequalities $L_c < L/2$ ($L_c > L/2$) are always valid, i. e. the rotation center is located farther from (closer to) the cyclonic core of the lower layer. When $L = L^* \approx 1.59$, we have $L_c = L/2$. This is demonstrated in Fig. 6c where we can observe of vortex trajectories for the three cases: $L < L^*$, $L = L^*$, and $L > L^*$.

In the limit $L \to 0$, the configuration composed of the collapsing lower-layer vortices and the upper-layer vortex located above them, rotates with theoretically infinite angular velocity. As $L \to \infty$, the vorticity center is situated in an infinitesimally small neighborhood the cyclonic vortex. This vortex hardly affects the anticyclonic vortices moved to infinity; the angular velocity of their rotation is infinitesimally small.

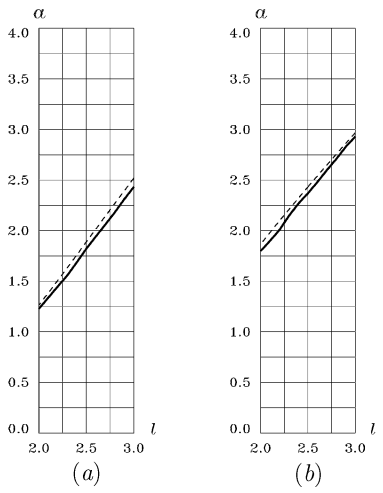

Fig. 7. Dependency equations $l_c(l)$ of the *Eccentric Roundabout* at $\gamma = 1$ and $\gamma = 2$ for the discrete (dashed line) and the finite-core (solid line) vortices. Markers correspond to the experiment conditions in Fig. 8.

3.2.2. Finite-core vortices

Unlike the case discussed in section 3.1.2, where the minimum value of $l = L/\gamma$ was equal to unity (as the unit radius of the vortex patches) now we have $lmin = 2$. This follows from the condition that one of the satellites is situated in the same layer as the core, and, as before, the configuration must have geometrical symmetry. It is obvious that such vortices are more stable. Moreover, unlike closely located vortices of the same sign of intensity, the intensities of the lower-layer vortices now are of different signs and, consequently, no merging will occur between them. Figure 7 shows the relationships between external parameters of the problem for two values of γ. In this figure $lc = L_c/\gamma$, and the dashed lines are identical to the corresponding curve section L_c in Fig. 6b. The solid lines for the finite-core vortices were obtained numerically. The figure shows that the model of the discrete vortices approximates well the distance between the centers of the finite-core vortices and that taking into account the fact that their sizes are finite is equivalent to the increase in stratification. Figure 8 shows four experiments on the evolution of vortex patches involved in motion of the *Eccentric Roundabout* type. In each experiment (8.1.a, 8.1.b, 8.2.a, and 8.2.b), the time interval between frames is approximately a quarter of the period. The figure shows that, in this particular case, for quite a wide range of external parameters the finite-core vortices qualitatively behave like the discrete vortices. This remains true even in the limiting cases when the bottom-layer vortices touch one another at the initial moment (Fig. 8.1.a and Fig. 8.2.a). However, the vortex patch system ceases to be Hamiltonian (in the first two cases, 9%, and 4% respectively, of the vortex area are lost through filamentation).

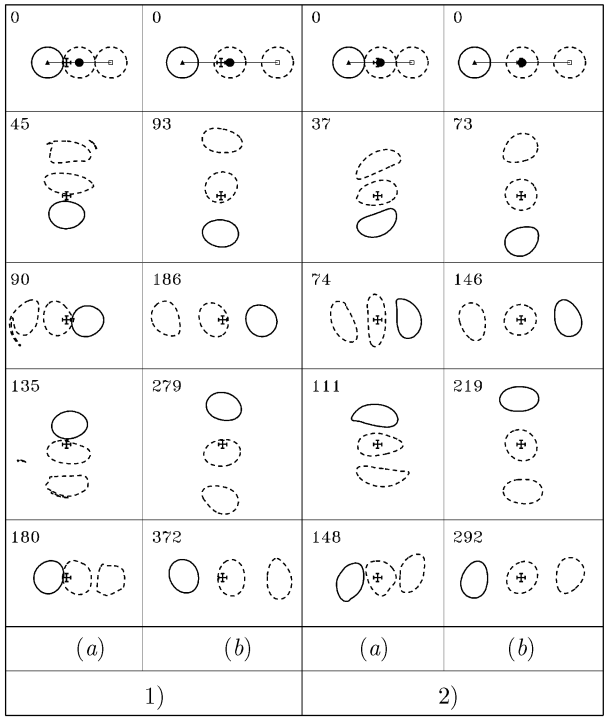

Fig. 8. Vortex-patch configurations composing a two-layer tripolar structure of the *Eccentric Roundabout* type. 1) $\gamma = 1$, 2) $\gamma = 2$; (a) $l = 2$, (b) $l = 3$.A cross marks the location of a vorticity center.

4. Analysis of the relative motion of three discrete vortices in the general case

Let $P \neq 0$. In this case, to analyse the relative motion, we introduce the trilinear coordinates [1]:

$$t_1 = -\frac{3\kappa_2^1\kappa_2^2(d_{22}^{21})^2}{|P|^2}, \quad t_2 = -\frac{3\kappa_1^1\kappa_2^2(d_{21}^{21})^2}{|P|^2}, \quad t_3 = -\frac{3\kappa_1^1\kappa_2^1(d_{21}^{11})^2}{|P|^2}. \tag{4.1}$$

Obviously,

$$t_1 + t_2 + t_3 = 3. \tag{4.2}$$

Figure 9 illustrates the geometrical meaning of the trilinear coordinates: for a fixed point of the plane, the numbers t_1, t_2, t_3 are the distances from the point to the straight lines that intersect to form rectilinear oriented triangles. The so-called *physical areas* (I) and (II) are also shown here. Inside them, the triangle rule is fulfilled, and takes the following form in coordinates (4.1):

$$(\kappa_1^1 t_1)^2 + (\kappa_2^1 t_2)^2 + (\kappa_2^2 t_3)^2 \leqslant 2(\kappa_1^1\kappa_2^1 t_1 t_2 + \kappa_1^1\kappa_2^2 t_1 t_3 + \kappa_2^1\kappa_2^2 t_2 t_3). \tag{4.3}$$

In case I, the assumption (2.4) is valid, and the conditions (4.3) may be written as follows:

$$12t_1 + (t_2 - t_3)^2 \leqslant 0 \quad \text{at} \quad t_1 < 0, \quad t_2 \geqslant 0, \quad t_3 \geqslant 0, \tag{4.4}$$

while for case II, the assumption (2.5) is valid, and instead of (4.3) we obtain:

$$12t_2 + (t_1 - t_3)^2 \leqslant 0 \quad \text{at} \quad t_1 > 0, \quad t_2 \leqslant 0, \quad t_3 \geqslant 0. \tag{4.5}$$

Level lines of the Hamiltonian (2.3) in the trilinear coordinates will coincide with the level lines of the functions

$$\begin{pmatrix} W_1 \\ W_2 \end{pmatrix} = \begin{cases} \ln\left(\dfrac{-t_1}{t_2 t_3}\right) - 2\left[K_0\left(\gamma\sqrt{\dfrac{-t_1|P|^2}{3\kappa^2}}\right) + 2K_0\left(\gamma\sqrt{\dfrac{t_2|P|^2}{6\kappa^2}}\right) + 2K_0\left(\gamma\sqrt{\dfrac{t_3|P|^2}{6\kappa^2}}\right)\right], \\ \ln\left(\dfrac{-t_2}{t_1 t_3}\right) + 2\left[2K_0\left(\gamma\sqrt{\dfrac{t_1|P|^2}{6\kappa^2}}\right) + K_0\left(\gamma\sqrt{\dfrac{-t_2|P|^2}{3\kappa^2}}\right) - 2K_0\left(\gamma\sqrt{\dfrac{t_3|P|^2}{6\kappa^2}}\right)\right]. \end{cases} \tag{4.6}$$

Here, W_1 is defined on the area (4.4) when conditions I are satisfied, and W_2 on the area (4.5) when conditions II are satisfied.

Examples of contour levels for functions W_1 and W_2 from (4.6) are given in Fig. 10.1 and Fig. 10.2, respectively. Motion of a representative point along a fixed level line of the function W_1 or W_2 with periodic "reflection" from the boundary of the physical area corresponds to the real evolution of the three-vortex system. A typical location of singular points is shown in Fig. 11; the points of the phase plane corresponding to the initial conditions of computations are also marked. The following general properties of the phase trajectories may be noted:

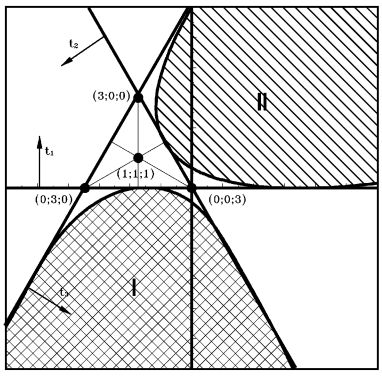

Fig. 9. Scheme of trilinear coordinates t_1, t_2, t_3 (their meaning being clear from the relations (4.1)–(4.2)). Ternaries of the coordinates in the parentheses correspond to the points marked by black circles. Dashed parts of areas I and II represent "physical areas" for the problems with conditions (2.4) and (2.5) and are defined by relations (4.4) and (4.5) respectively.

(a) All phase curves start and end at the boundary of the physical area. This means that 1) all relative vortex motions are periodic; 2) during one period the vortices form a collinear configuration twice. In particular, reliable information about possible relative motions of the vortex system can be obtained by placing all the three vortices on the same straight line at $t = 0$. Their motion is studied over one period.

(b) Motions of the three-vortex system can be qualitatively divided into three types: {1}, {2} and {3}. The initial collinear vortex configuration determines to which of these types the motion belongs.

(c) A phase portrait can have singular points of elliptic (e) or hyperbolic (h) types (Fig. 11).

The phase portraits provide complete information about the relative motion of the vortex system. Nevertheless, the analysis of relative motion may not reflect all the features of the absolute vortex motion[7]. We will examine numerically the main distinguishing characteristics of their behavior.

5. Absolute motion of the three-vortex system

According to property (a), consider the simplest initial (reference) position of the vortices x_1^1, x_2^1, x_2^2 along the x-axis such that $\tilde{x}_1^1 = \tilde{x}_2^1 = 0$ and with the lower-layer vortex $\binom{1}{2}$ placed exactly below the upper-layer vortex $\binom{1}{1}$, and $\tilde{x}_2^2 \neq 0$. In this case, the value of the momentum P of the vortex system

[7]In [60], a stationary state of a four-vortex system in a two-layer fluid was found: two upper-layer vortices perform a centrally symmetric periodic motion along a closed quasi-elliptic trajectory; the two lower-layer vortices oscilate nutationally with respect to some immovable peripheral points which are also placed to form a configuration with point symmetry. In the phase portrait nothing special can be noticed about this periodic solution.

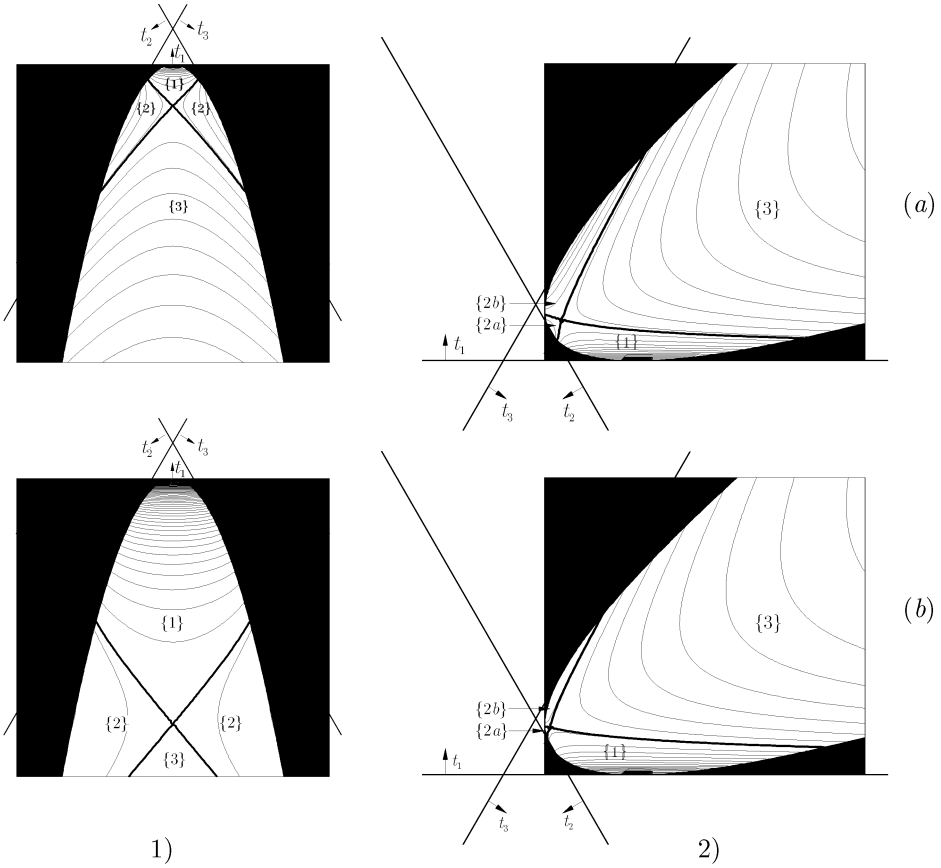

Fig. 10. Phase portraits of the relative three-vortex system motion in the two-layer fluid under the conditions I — Fig. 10.1 and II — Fig. 10.2 with different values for total momentum: $\gamma|P| = 1.7$ — (10.1.a); $\gamma|P| = 0.6$ — (10.1.b); $\gamma|P| = 5.0$ — (10.2.a); $\gamma|P| = 3.0$ — (10.2.b).Thick lines represent separatrices, which separate the parts of the phase plane, corresponding to the different types of the vortex interaction; their distinguishing properties are explained in the text. "Non-physical" parts of the phase plane are blackened. A picture of the corresponding trilinear axes is also shown here.

is completely determined by the initial position of the lower-layer vortex $\binom{2}{2}$. With respect to the coordinate sets

$$x_1^1 = \tilde{x}_1^1, \quad x_2^2 = \tilde{x}_2^2 + x_0, \tag{5.1}$$

$$x_2^1 = \tilde{x}_2^1 - x_0 \quad \text{in case} \quad I, \tag{5.2}$$

$$x_2^1 = \tilde{x}_2^1 + x_0/2 \quad \text{in case} \quad II, \tag{5.3}$$

the value of P remains the same for any x_0. In addition to x_0 and x_n^m we will also use the notation $X_0 = \gamma x_0$ and $X_n^m = \gamma x_n^m$. It may be seen from (4.1) that all the conclusions made from the analysis of the phase characteristics are valid with respect to these coordinates if, instead of the value P, we take the value γP. Any series of numerical experiments with the initial coordinate sets (5.1) and (5.2), or (5.1) and (5.3) will correspond to the actual phase portrait (e.g., one of the frames in Fig. 10). Below, a correlation is made between the peculiarities of vortex behavior and the characteristics of the phase curves. The illustrations show vortex trajectories. The trajectories (and the discrete vortices at some moment of time) are shown in the pictures in the following way: solid line and triangle =

the upper-layer vortex $\binom{1}{1}$; long dash and circle = the vortex $\binom{1}{2}$; small dash and square box = the vortex $\binom{2}{2}$. As before, the size of the marker indicates the intensity of the corresponding vortex. In the captions for the figures showing the trajectories of the discrete vortices, the following notation is used: $t = (t_1, t_2, t_3)$. In all the figures (except Fig. 24.1.a), the vortex configuration moves downwards. The previous notation for finite-core vortices is preserved.

5.1. Dynamics of arch-shaped vortices: Case *I*

5.1.1. Discrete vortices

Let $\kappa = 1$, hence, according to (4), $\kappa_1^1 = -2$, $\kappa_2^1 = \kappa_2^2 = 1$, and the initial conditions are given by relations (5.1)–(5.2). Specific phase portraits are shown in Fig. 10.1.a and Fig. 11a. In this case, they are symmetrical with respect to the straight line $t_2 = t_3$, because these variables are proportional to the squared distances between the anticyclone of the upper layer and the identical cyclones of the lower layer.

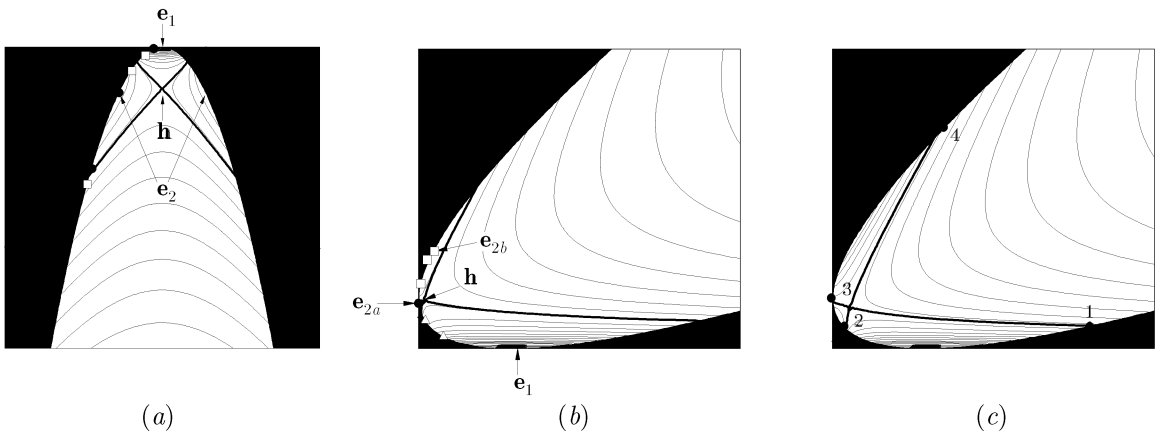

Fig. 11. Phase portraits and indication of singular points and points corresponding to the conditions of the numerical experiments shown in Figs. 12, 14 and 18:(a) $\gamma|P| = 1.7$ and the fulfillment of condition I; (b) $\gamma|P| = 3.0$ and the fulfillment of condition II;(c) $\gamma|P| = 5.0$ and the fulfillment of condition II.

Typical examples of the three types of motions are given in Fig. 12. For type $\{1\}$ (Fig. 12a), interaction between lower-layer vortices prevails, while the anticyclonic vortex executes only insignificant oscillations. A motion of this type may be characterized by the formula

$$\binom{1}{2}\binom{2}{2} + \binom{1}{1}. \tag{5.4}$$

In this case, the vortex system moves perpendicularly to the x-axis. The lower-layer vortices rotate in the cyclonic direction around the center that moves in a straight line in such a way that every one-half period they exchange places as soon as they are in collinear positions.

The peculiarity of motion of type $\{2\}$ (Fig. 12b) is that the interaction between the upper-layer vortex and one of the lower-layer vortices prevails (the one closest to it at the initial moment). During this motion, the anticyclonic rotation, induced by the upper-layer vortex, captures the cyclone located in the bottom layer. The following formulae represent such motions:

$$\binom{1}{1}\binom{1}{2} + \binom{2}{2} \quad \text{and} \quad \binom{1}{1}\binom{2}{2} + \binom{1}{2}, \tag{5.5}$$

they correspond to the left and the right parts of the area $\{2\}$ on the phase portrait, respectively. The result of computations according to the first formula in (5.5) is shown in Fig. 12b.

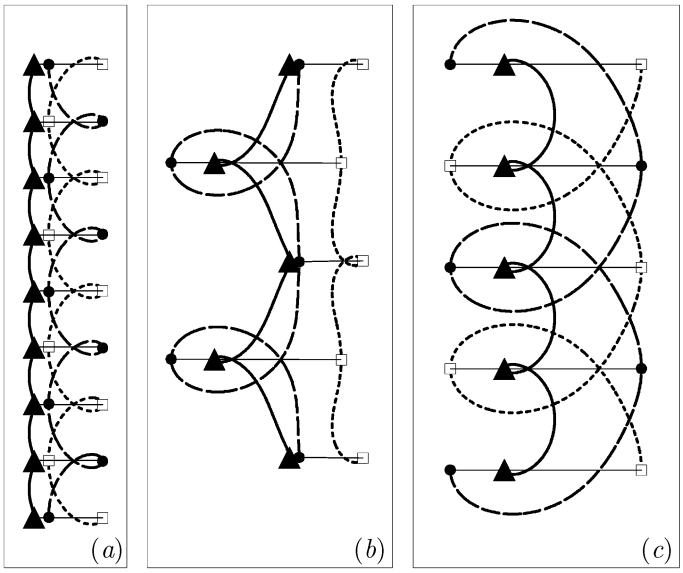

Fig. 12. Trajectories of the absolute motion of the discrete vortices at $\gamma P = 1.7$. Initial conditions are defined by the formulae (5.1)–(5.2) at $\tilde{X}_1^1 = \tilde{X}_2^1 = 0$, $\tilde{X}_2^2 = 1.7$, and:$X_0 = -0.3$; $t = (-1.2561; 4.0692; 0.1869)$ — (a); $X_0 = -0.2$; $t = (-1.7543; 4.6713; 0.0830)$ — (b); $X_0 = 1.1$; $t = (-15.7889; 16.2768; 2.5121)$ — (c). White box markers correspond to the experimental conditions in Fig. 11a.

Finally, type $\{3\}$ solutions, according to the Fig. 12a, are characterized by anticyclonic rotation of all the three vortices:

$$\binom{1}{1}\binom{1}{2}\binom{2}{2}. \tag{5.6}$$

This is due to the predominant (and capturing) role of the upper-layer vortex.

Remark 3. The cyclicity periods of upper- and lower-layer vortices are 1:2 for motions of types $\{1\}$ and $\{3\}$, while in case $\{2\}$ they coincide. This can be explained by the fact that every phase curve of types $\{1\}$ and $\{3\}$ has a mirror symmetry property, while those of type $\{2\}$ — do not.

Remark 4. Depending on the value of the vortex-system momentum, the points where the t_2- and t_3-axis touch the boundary of the physical area belong either to region $\{2\}$ (Fig. 10.1.a) or to region $\{1\}$ (Fig. 10.1.b). It is obvious that the initial vortex positions correspond to these situations when $x_0 = 0$ in (5.1)–(5.2).

Examples of such motions are shown in Fig. 13. Figure 13a illustrates a motion of type $\{2\}$ over one period. It is clear that in this case the vortex $\binom{1}{2}$ can start its motion only under the influence of the second vortex $\binom{2}{2}$ from the bottom layer, but it is captured immediately by the upper-layer vortex, and then the entire configuration moves according to scenario $\{2\}$. A motion of type $\{1\}$ on the same time interval is shown in Fig. 13b. During this time, more than ten periods were completed. In this figure, the markers and the line-segments that connect them, indicate not only collinear states, but also the final vortex positions. It my be seen that in every one-half period the lower-layer cyclones in turn find themselves exactly beneath the anticyclone of the upper layer. The examples given in Figs. 12 and 13 represent the conditions when the corresponding phase curves pass away from the separatrices and the singular points. Let us now examine the properties of the stationary solutions represented by the singular points.

The region around the point $e1$ (see Fig. 11) corresponds to closely located lower-layer vortices. At the same time, the lower-layer vortices must rotate around their common center with theoretically infinite angular velocity. Interlayer interaction hardly exists in this case, and manifests itself only in the form of translational motion of the configuration as a whole. In the limiting situation, we have a

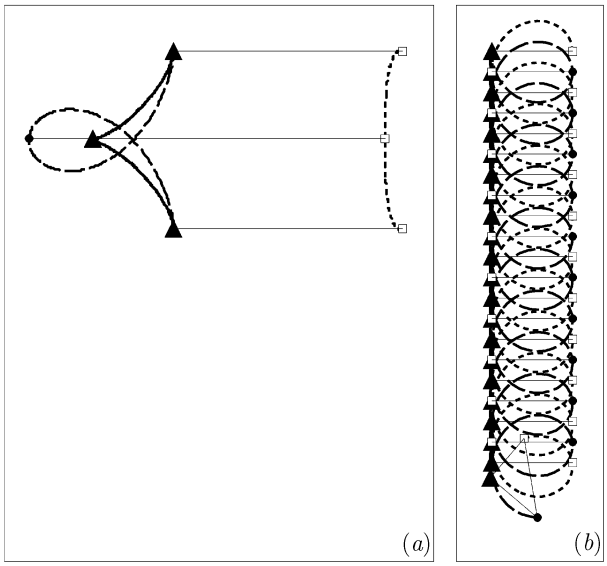

Fig. 13. The same as in Fig. 12, but at $X_0 = 0$; $t = (3; 6; 0)$ and $\gamma P = 1.7$ — (a); and $\gamma P = 0.6$ — (b).

structure equivalent to a two-layer pair of vortices with intensities in the upper and lower layers of -2κ and 2κ respectively. An example of motion with parameters close to those described above is given in Fig. 14a (during the time interval on which the solution was numerically obtained, lower-layer vortices performed 66 revolutions; we placed markers only at the initial and final collinear vortex positions not to embark the figure with unnecessary details). In this figure, at the initial moment, γd_{22}^{12} equals to 0.5, and thus is not small. However, even for such significant parameter values, the lower-layer vortex trajectories are hard to observe. For γd_{22}^{12} less than 0.5 the picture becomes unreadable, and, therefore, we do not show here the corresponding results.

Let us now examine one of the points e_2, belonging to the boundary of the physical area (see Fig. 11a). It is known [11] that collinear configurations composed of three vortices and corresponding to such singular points must rotate as a whole around the vorticity center. A remarkable (and unexpected) property of the *two-layer* configuration is the presence of these elliptic points under the condition that *the angular momentum of the system is not zero*. The vorticity center is shifted to infinity, so that the three-vortex collinear configuration, like a vortex pair, must move uniformly and rectilinearly in the direction perpendicular to the straight line where the vortices were placed (an example is given in Fig. 14b). Since a function which is identically constant may be considered as a periodic function with arbitrary period, the horizontal rectilinear segments only join the initial and the final vortex positions in this part of the figure. This solution is stable (small deviations of the initial coordinates from their stationary positions cause insignificant periodic deviations of the trajectories from the straight lines). By anology with the term *heton* and in view of the fact that this structure has *three* cores, we will call it *triton*. Triton can be used as the simplest model of the vortex structure known as *modon + rider* [21].

Obviously, to the hyperbolic point h there corresponds an unstable solution. A configuration in the form of an isosceles triangle ($t_2 = t_3$), with the upper-layer vortex placed in the specified vertex of the triangle, corresponds to the unstable solution and moves progressively in the direction parallel to the base of the triangle. This is proved in Fig. 14c, where the trajectories of the vortex system are shown. For this system, the representative point of the phase plane is initially located at the boundary of the physical area in the vicinity of the point at which the separatrice originates. In this figure, the markers and the segments linking them indicate not only collinear, but also other synchronous intermediate vortex configurations (the internal areas of such triangular structures are hatched) on the time

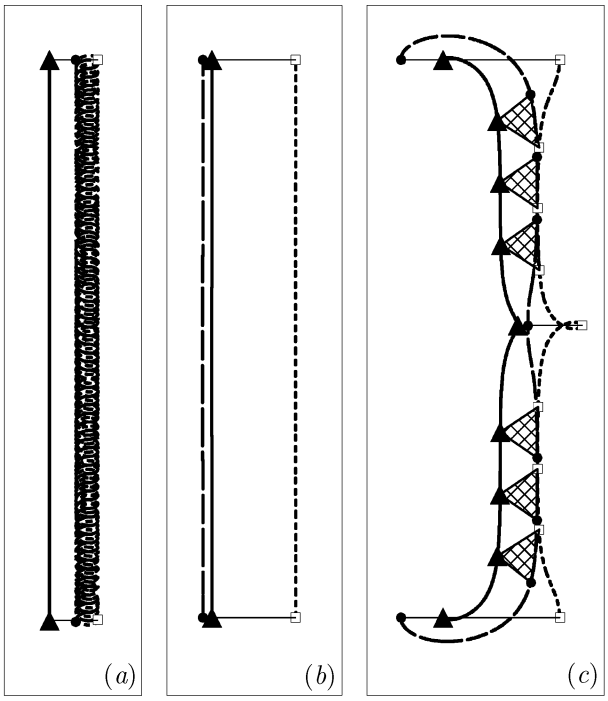

Fig. 14. The same as in Fig. 12, but at: $X_0 = -0.6$; $t = (-0.2595; 2.5121; 0.7474)$ — (a); $X_0 = 0.2062; t = (-4.6321; 7.5438; 0.0883)$ — (b); $X_0 = 0.9611$; $t = (-13.6197; 14.7020; 1.9177)$ — (c). Circular markers correspond to the experimental conditions in Fig. 11a.

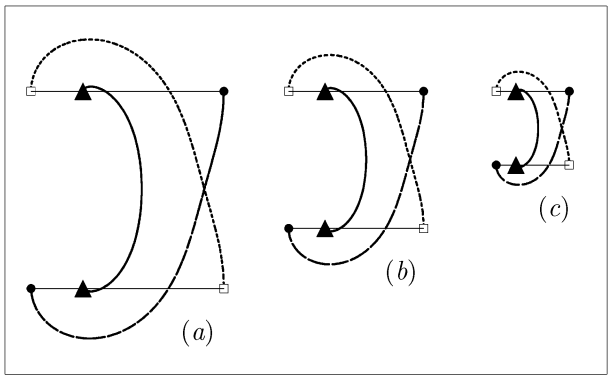

Fig. 15. Trajectories of the absolute motion of the discrete vortices at $\gamma P = 1.7$, $X_0 = 1$; $t = (3.7184; -0.9900; 0.2716)$: (a) $\gamma = 0.70$; (b) $\gamma = 1.00$; (c) $\gamma = 1.85$.

intervals during which the representative point belongs to a very small neighborhood of the separatrice intersection point h. It is clear that these unstable configurations cannot exist permanently and, as shown in the figure, they exchange positions when they pass the collinear states as follows:

$$\binom{1}{2}\binom{1}{1}\binom{2}{2} \to \binom{2}{2}\binom{1}{1}\binom{1}{2} \to \ldots \tag{5.7}$$

Remark 5. Since the total momentum value is fixed, the type of the motion of the vortex structure is governed by *one* geometrical parameter. Thus, for case I, it is convenient to use the parameter $Z = |2X_0 + \gamma P|$. It is clear that, at $Z = 0$, the vortices of the bottom layer merge. If, for example, $\gamma P = 1.7$,[8] for $Z \in (0; 0.6202)$, $(0.6203; 1.1812)$, and $(1.1813; \infty)$, we have motions of types $\{1\}$, $\{2\}$, and $\{3\}$, respectively.

[8]Specific trajectories of the absolute motion for this value of total momentum are shown in Fig. 12–14.

5.1.2. Finite-core vortices

Let us now examine only one of the numerous aspects of the motion of finite-core vortices. The role of the parameter γ in the dynamics of finite-core vortices will be illustrated by an example.

If $\gamma P = 1.7$ and $X_0 = 1$, then $Z = 3.7$, and, in accordance with Remark 5, the discrete vortices can perform only motions of type $\{3\}$. We will now compare the computation results obtained for the discrete and finite-core vortices for the same geometric parameters but for three different values of the stratification parameter γ. Thus, Fig. 15 shows a half-period picture of the discrete vortex trajectories with the parameter γ increasing. It is obvious that they can be similar and are described by formula (5.6).

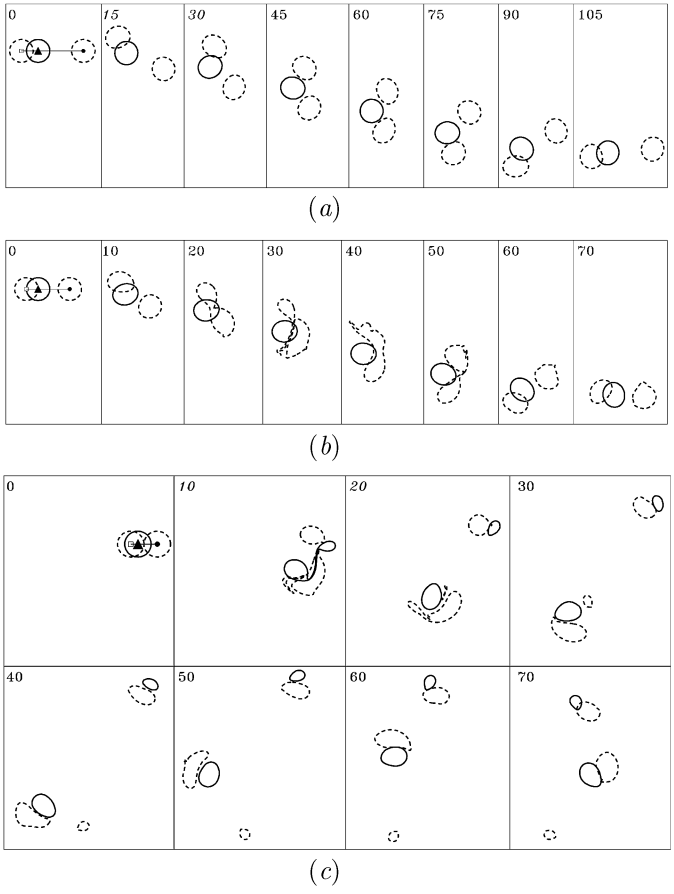

Fig. 16. Synchronous pictures of the vortex-patch contours at the same parameter values as in Fig. 15: (a) $\gamma =$ $= 0.70$; (b) $\gamma = 1.00$; (c) $\gamma = 1.85$.

Figure 16 demonstrates the behavior of vortex patches with the same parameter values and the time interval close to one-half period. When $\gamma = 0.7$, (Fig. 16a) the centers of the vortex patches behave as discrete vortices, and the shape of the vortex boundaries, as they evolve, remains generally circular. When $\gamma = 1$ (Fig. 16b), they temporarily merge during the vortex "rapprochement" stage in the bottom layer. Then they disintegrate into two unequal parts (the area ratio is 1:0.86), 1.1% of their mass being lost through filamentation. The vortex system, as a whole, develops according to the the type $\{3\}$ scheme. Finally, in the case shown in Fig. 16c, when $\gamma = 1.85$, we see the disintegration of the unstable vortex structure. In the lower layer, vortex patches merge and then split into three parts. The upper-layer vortex also splits into two unequal parts. Later (this shown in the upper part of the figure), the vortices regroup to form a dipolar structure representing a two-layer vortex with

tilted axis ($S_1^1\Pi_1^1 = -1.54$; $S_2^1\Pi_2^1 = 1.96$); and a tripolar structure representing a core in the upper layer and two satellites in the bottom layer ($S_1^2\Pi_1^2 = -4.54$; $S_2^2\Pi_2^2 = 2.97$; $S_2^3\Pi_2^3 = 0.72$), as shown in the lower part of the figure. The total vorticity of each structure determines their direction of rotation, namely, cyclonic for the first structure and anticyclonic for the second. It is clear that this type of motion has no analogs in the discrete-vortex approximation.

REMARK 6. Let us note that when $\gamma = 1.85$ (Fig. 16c), the lower-layer vortex patches touch one other, thereby indicating that for the given value of the total momentum ($\gamma P = 1.7$), the maximum value of γ is 1.85.

5.2. Dynamics of arch-shaped vortices: Case *II*

5.2.1. Discrete vortices

If we suppose, as in the previous case, that $\kappa = 1$, we obtain, according to (5), $\kappa_1^1 = \kappa_2^2 = -1$, $\kappa_2^1 = 2$. When this takes place, and despite the fact that the total intensity of the vortex system still remains zero, the laws of interaction between the stronger cyclonic vortex $\binom{1}{2}$ and the two equal anticyclones in the upper and lower layers are different (as mentioned in subsection 3.2.1). It is also obvious, that the upper layer vortex $\binom{1}{1}$ has to interact in a different way with the lower-layer vortices $\binom{1}{2}$ and $\binom{2}{2}$, because now they have different intensities (both in sign and value). This non-equivalence in interaction reflects an asymmetry of the phase curves with respect to the straight line $t_1 = t_3$, which is (in this case only) the axis of symmetry for the physical area boundary. This situation also influences the properties of each selected type of motion. Let us now examine these types.

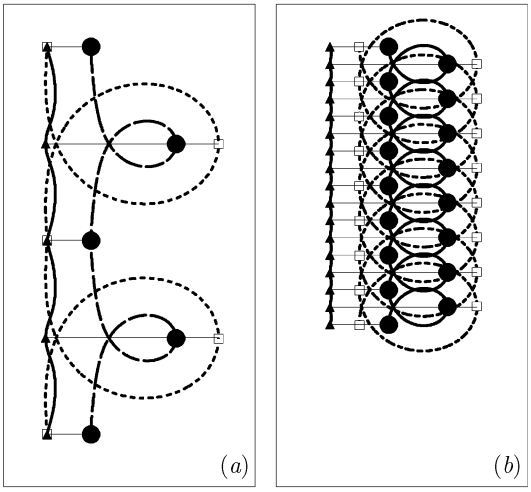

Fig. 17. Trajectories of the absolute motion of the discrete vortices at $\gamma P = 3$. Initial conditions are defined by the formulae (21), (23) at $X_2^2 = -3$: $X_0 = 3$; $t = (1.5; 0.0; 1.5)$ — (a); $X_0 = 4$; $t = (0.6667; -0.3333; 0.6667)$ — (b). Phase curves belong to the area $\{1\}$ in Fig. 10.2.b. Circular white markers correspond to the experimental conditions in Fig. 11b.

Two examples (evaluated numerically) for type $\{1\}$ motion are given in Fig. 17. As in case *I*, the motions described by (5.4) in which the intra-layer interaction prevails are of type $\{1\}$. It is clear that the bottom-layer vortices now perform an anticlockwise collective rotation caused by the strongest cyclonic vortex. In the experiment shown in Fig. 17a, the initial condition is $t_2 = 0$ (the point at which the physical-area boundary touches the axis t_2). As a consequence, the anticyclonic vortices of the upper and lower layers periodically appear on the same vertical line, thus forming quasi-barotropic constructions.

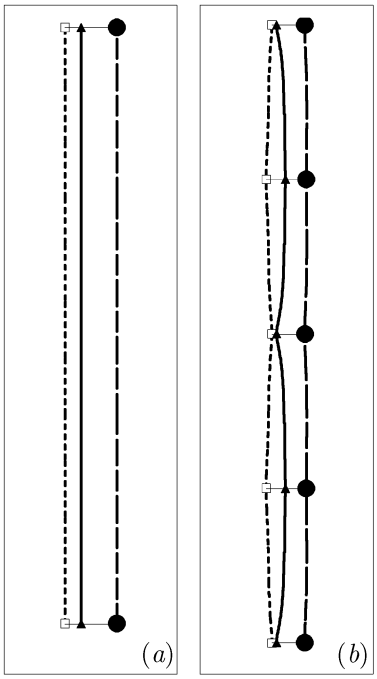

Fig. 18. The same as in Fig. 17, but at: (a) $X_0 = 2.441$; $t = (2.1111; -0.1042; 0.9931)$; (b) $X_0 = 2.77$; $t = (1.7388; -0.0176; 1.2788)$.Phase curves belong to the area {2a} in Fig. 10.2.b. A circular marker corresponds to the experimental conditions in Fig. 11b.

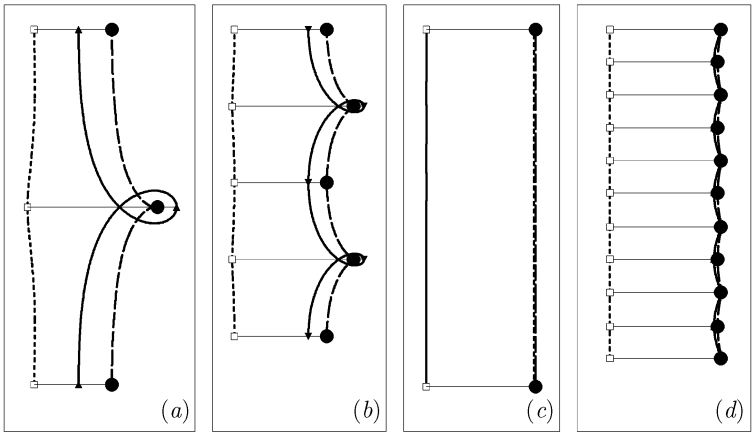

Fig. 19. The same as in Fig. 17, but at: (a) $X_0 = 1.8$; $t = (2.94; -0.48; 0.54)$; (b) $X_0 = 1$; $t = (4.1667; -1.3333; 0.1667)$; (c) $X_0 = 0.085$; $t = (5.8312; -2.8324; 0.0012)$; (d) $X_0 = 0; t = (6; -3; 0)$. The phase curve belongs to the area {2b} in Fig. 10.2.b. White box markers correspond to the experimental conditions in Fig. 11b.

The motions of type {2} fall into two subtypes, {2a} and {2b}. Subtype {2a} includes those motions where the interaction of the anticyclonic vortices from the different layers is the greatest, while subtype {2b} includes those where the capture of the upper-layer anticyclone by the strongest lower-layer cyclone takes place. Nevertheless, as in the previous section, type {2} is characterized as

a whole by formulae (5.5). Detailed examples are given in Fig. 18[9] and Fig. 19; translational collinear constructions of the triton type are shown for each of these subtypes in Fig. 18a and Fig. 19c (to these constructions correspond the points e_{2a} and e_{2b} in Fig. 11b). Since the motion starts at the reference state (at $t_3 = 0$), Fig. 19d demonstrates the effect of the periodic restoration of a structure composed of a cyclonic lower-layer vortex and a non-compensated two-layer vortex whose axis is vertical and the directions of rotation in the layers are opposite.

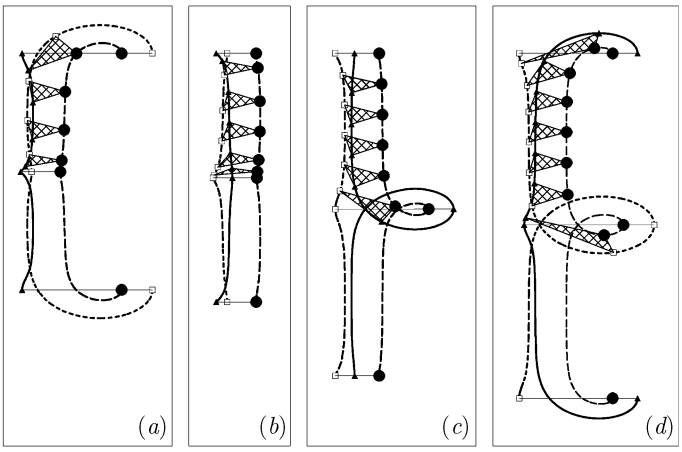

Fig. 20. Trajectories of the absolute motion of the discrete vortices at $\gamma P = 5$. Initial conditions are defined by the formulae (5.1) and (5.3) at $X_2^2 = 5$: (a) $X_0 = 14.4791$; $t = (1.2037; -10.7824; 12.5787)$ — the phase curve belongs to the area {1} in Fig. 10.2.a;(b) $X_0 = 5.7910$; $t = (1.0629; -0.0751; 2.0121)$ — the phase curve belongs to the area {2a} in Fig. 10.2.a; (c) $X_0 = 3.5886$; $t = (2.4666; -0.2391; 0.7726)$ — the phase curve belongs to the area {2b} in Fig. 10.2.a; (d) $X_0 = -3.6126$; $t = (11.1183; -8.9014; 0.7831)$ — the phase curve belongs to the area {3} in Fig. 10.2.a. The points "1"–"4" in Fig. 11.c correspond to the initial conditions of the numerical experiments in the fragments (a)–(d).

In contrast to the case studied in section 4.2, type {3} motions are characterized here by the cyclonic rotation of the whole system, induced by the strong vortex of positive intensity in the bottom layer. This effect is demonstrated in Fig. 20d. Formula (5.6) is valid for this type of interaction.

Figure 20 shows examples of all types of motion together with their limiting cases, when the phase curves in the plane of the parameters (t_1, t_2, t_3) belong to the vicinity of the separatrices, and the points 1, 2, 3, and 4 in Fig. 11c (motions of types {1}, {2a}, {2b} and {3}, respectively) represent the initial conditions. Each fragment gives a one-period trajectory. The series of triangular configurations formed over the intervals when the representative point is in the vicinity of the singular point h are shown only for the first half of the period. It is clear that the initially collinear configurations in Figs. 20b, 20c, 20d practically repeat the configurations shown in Figs. 20a, 20b, 20c respectively, with the time-shift $T/2$ (T is the period), because the corresponding positions of the representative points on the phase plane are very close, despite the fact that they are located on different sides of the phase points where the separatrices intersect the boundary of the physical area.

Remark 7. It is possible to single out two particular types of structures able to move forward among the set of all possible non-collapsing three-vortex motions in a two-layer fluid. These are the stable collinear configurations (tritons), corresponding to the elliptic singular points e_2 of the phase plane, and the unstable triangular structures for the hyperbolic point h. When the condition (2.4) is fulfilled, the limit (symmetrical) triangular vortex formation represents an isosceles triangle, and in the case when condition (2.5) is valid — a scalene triangle.

[9]In the plane (t_1, t_2, t_3), the phase coordinates of the initial vortex positions (as well as the phase curves) are close to those in both experiments given in Fig. 18 (they are so much close that in Fig. 11b one circular marker covers them). This observation is also valid for the upper box marker in Fig. 11b, relating to the Figs. 19c and 19d.

REMARK 8. Since a strong intra-layer interaction is the main distinguishing property of motions of type {1}, while the interaction between the layers typifies type {3} motions, these types of motions may be regarded as a generalization of the tripolar structures IR and OR (see section 3, where $P = 0$) to the case $P \neq 0$. For comparison, these cases are summarized in Table 1.

Table 1

Property	Type of two-layer vortex	
	Roundabout ($P = 0$)	Arbitrary arch-shaped vortex ($P \neq 0$)
Translational movement	absent	present
Rotation of the vortex structure	with constant angular velocity	with variable angular velocity
Collinearity	always observed	periodically observed (every half period)

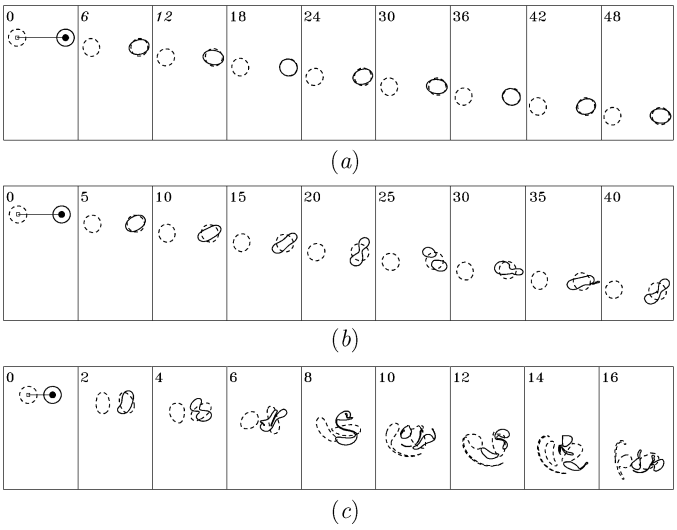

Fig. 21. Synchronous pictures of the vortex-patch contours at $\gamma P = 5$ and $X_0 = 0$: (a) $\gamma = 0.9$; (b) $\gamma = 1.0$; (c) $\gamma = 1.8$.

5.2.2. Finite-core vortices

Figure 21 illustrates a series of vortex patch configurations with the reference initial state (see the beginning of section 5). In this case, the anticyclonic vortex of the upper layer is situated above the bottom cyclone. According to Fig. 10.2.a, the conditions for the existence of type {2a} motions are fulfilled for discrete vortices. Figure 21a shows that for $\gamma < 1$ the finite-core vortices qualitatively behave as discrete vortices (compare with Fig. 19d). With slightly less stratification ($\gamma = 1$, Fig. 21b), the vortex construction $\binom{1}{1}\binom{1}{2}$, initially representing a two-layer vortex with vertical axis, becomes unstable. When this happens, the upper-layer vortex patch splits into two parts which later merge again. If computations are performed on a long-time interval, such as in the case shown in the figure, this process repeats periodically. The shape of both bottom vortex patches remains almost circular all the time.

As the parameter γ grows (Fig. 21c) the role of interaction between the lower-layer vortices increases: the vortex $\binom{2}{2}$ gets involved in the rotational motion around the strong cyclone (mainly

through the thin thread filamentation). The desintegration of the vortex patch in the upper layer occurs quickly and more effectively than in the previous case. The bottom cyclone remains the most conservative.

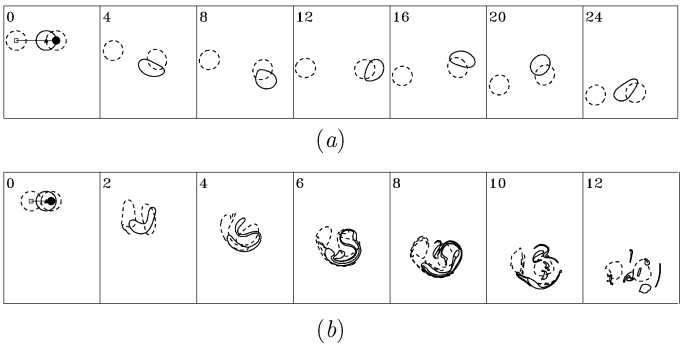

Fig. 22. The same at $X_0 = 2$: (a) $\gamma = 1$; (b) $\gamma = 2$.

Figure 22 shows another two examples of finite-core vortex motions of type {2a} when the characteristic discrete vortex trajectories have the form shown in Fig. 19a and 19b. Since stratification is moderate ($\gamma = 1$, Fig. 22a), the finite-core vortices behave as discrete vortices, and the first of the formulae (5.5) is valid. Only an insignificant deformation of the upper-layer contour is observed. At $\gamma = 2$, when the upper- and lower-layer vortex boundaries are in contact at the initial moment, the upper-layer vortex almost decays, and interaction between bottom vortices becomes more active. It is clear that in this case the vortex structure significantly differs from its discrete analog.

5.3. Analysis of partial solutions

Let us now identify the general conditions for the existence of stationary solutions for the case of discrete vortices (such as a triton and a symmetrical triangular configuration) for arbitrary values of the system momentum.

5.3.1. Collinear configuration — triton (discrete vortices)

Let us now assume that all the three vortices are initially placed on the x-axis. The upper-layer vortex $\binom{1}{1}$ situated at $x = 0$, finds itself between the two others with the vortex $\binom{1}{2}$ being to the right of it. The distance between the vortices $\binom{1}{2}$ and $\binom{2}{2}$ equals $2L$ as before. Denote $|X_2^2| = \gamma d_{12}^{12}$ by A (see Figs. 23a and 23b). The equations of motion (2.1)–(2.2) are used to obtain the conditions for the structure to move as a solid body in the direction of the y-axis with constant velocity:

$$\frac{A^2 - 2AL + 4L^2}{2AL(2L - A)} = K_1(A) + K_1(2L - A) + K_1(2L). \tag{5.8}$$

This equation may be regarded as a dispersion relationship that can be used to find the geometric parameters of the translational collinear solutions for tritons. It is important to note that equation (5.8) is valid in both conditions I and II. At the same time, the corresponding translation velocities V_1 and V_2 of these configurations are different:

$$\begin{pmatrix} V_1 \\ V_2 \end{pmatrix} = \frac{\kappa\gamma}{4\pi}\left[\left(\frac{1}{A} - K_1\Big(A\Big)\right)\begin{pmatrix} 1 \\ -1 \end{pmatrix} - \left(\frac{1}{2L - A} - K_1\Big(2L - A\Big)\right)\begin{pmatrix} 1 \\ 2 \end{pmatrix}\right] \equiv \frac{\kappa\gamma}{4\pi}\begin{pmatrix} F1 \\ F2 \end{pmatrix}. \tag{5.9}$$

As the expressions in parentheses on the right-hand side of this equation are non-negative, it is obvious that, for any A, we have $V_2 < 0$, and $|V_2| > |V_1|$. Moreover, since the dispersion relation (5.8)

is fullfilled, we get $V_1 > 0$ (< 0) for $A > L$ ($A < L$). The sign of V_2 is predetermined by the choice of the initial vortex location, namely by the assumption that the vortices $\binom{1}{2}$ and $\binom{2}{2}$ have positive and negative x-coordinates, respectively. If in case II we interchange the positions of the lower-layer vortices, the velocity vector of the triton will take the opposite direction. If $A < L$ or $A > L$, and $L \to \infty$, we have $A \to 0$ or $A \to 2L$, respectively. In this case the coordinates of one of the bottom vortices and of the upper-layer vortex coincide. Constructions with zero limit velocity values V_1 and V_2 correspond to these conditions. At the same time, V_1 has two extrema at $L \approx 1.70$ when $A \approx 0.02$ and $A \approx 3.38$, and V_2 has one extremum, taking its minimum value at $A = L_0$.

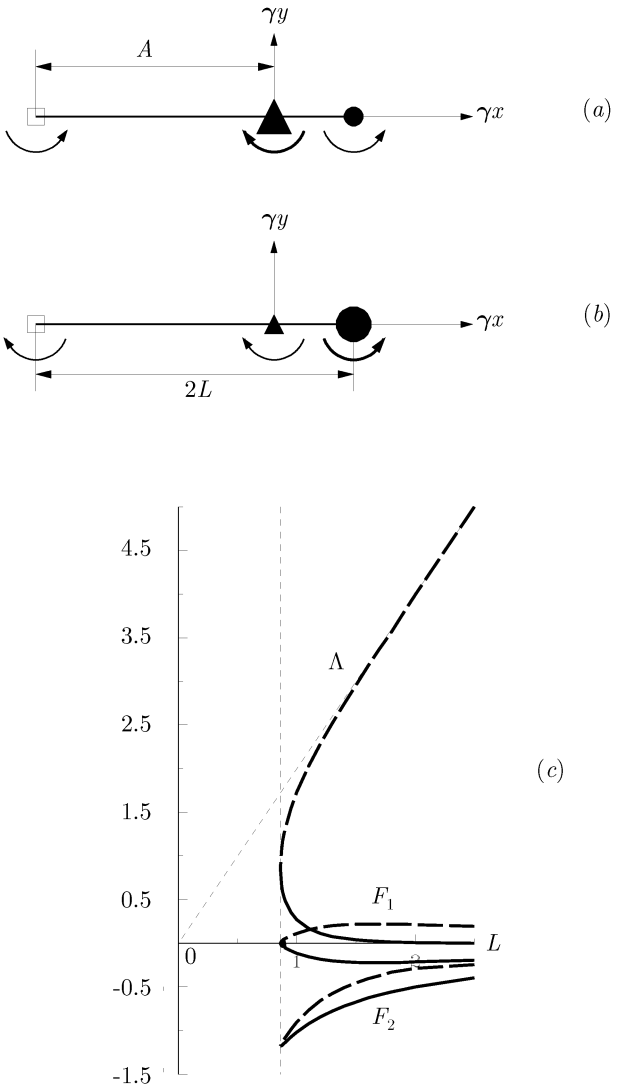

Fig. 23. Characteristics of the collinear construction of the three-vortex system: (a) Scheme of the initial vortex dislocation in case I; (b) The same for case II; (c) Dispersion curve $A(L)$ as a solution of equation (5.8) and corresponding dependencies $F_1(A)$, $F_2(A)$ on (5.9). Solid (dashed) lines correspond to branches of the functions with condition $A < L$ ($A > L$).

Figure 23c demonstrates the behavior of both the dispersion curve $A = A(L)$ and the relations (5.9). The thin dashed lines correspond to $L = L_0$ and $A = 2L$.

A triton always has the Λ-shaped structure; this means that in the vertical section, the anticyclonic

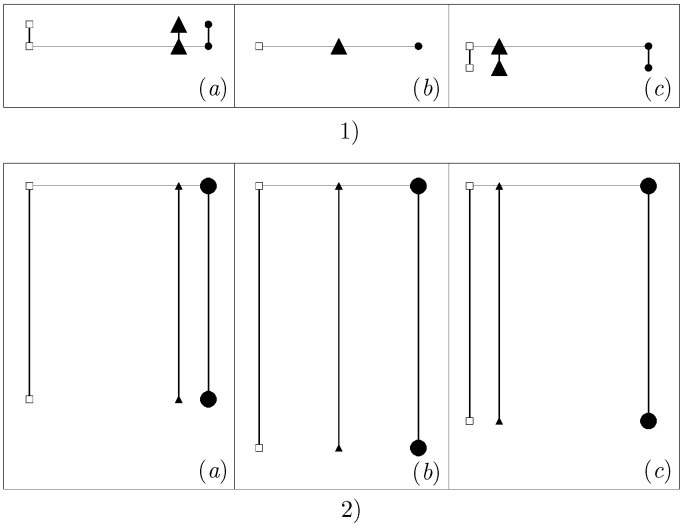

Fig. 24. Trajectories of the vortices composing a collinear configuration triton:1) under condition I; 2) under condition II;a) $A = 0.4$; b) $A = L_0 = 0.8602$; c) $A = 1.4587$.

vortex of the upper layer occupies the intermediate position between the vortices of the lower layer. However, if in case I, both pheriferal vortices are cyclones, and each of the three vortices induces a local deformation of the layer interface directed downward [31], in case II the cyclone of the bottom layer is located on one side of the configuration with two anticyclones — upper- and lower-layer ones — on the other side. In this situation, flexure of that layer interface, directed upward, develops over the anticyclonic vortex of the bottom layer.

Figure 24 demonstrates both kinds of triton motions for the three cases ($A > L_0$, $A = L_0$, and $A < L_0$). All the experiments were carried out over the same time interval and match Fig. 23c and formula (5.9). This allows us to get qualitatively the A-dependence of the velocity V_1. In particular, it can be seen that V_1 changes the sign at the point $A = L_0$, and $|V_2| > |V_1|$ for any A.

As mentioned above (concerning the vortex-roundabout, section 3), qualitative properties of a discrete-vortex system depend on the product of the stratification parameter γ and linear distance scales. In this case, they are the quantities $A = \gamma d_{12}^{12} = \gamma |x_2^2|$ and $L = \gamma l$, where l is a half distance between the bottom layer vortices. The role of the parameter γ in the formation of new structures becomes clear when we examine vortices of finite core.

5.3.2. Collinear configuration (finite-core vortices)

Suppose that the initial configuration consists of circular vortices of unit radius whose centers are located in accordance with I or II. Only by numerical experiments it is possible to find out whether or not the given configuration belongs to the triton class. The results of the corresponding computations are shown in Fig. 25, where the two pairs of dispersion curves are plotted as functions of the variables $(|x_2^2|, x_2^1)$ for both discrete and finite-core vortices. The values of the parameter γ are indicated in the figure. The shaded triangles indicate the area of geometric parameters where isolated vortex patches of the bottom layer cannot exist (the distance between their centers is less than 2). The straight line $|x_2^2| = x_2^1$ is the axis of symmetry for all the curves. As shown in the figure, if we take into account the finiteness of the vortex size, this is equivalent, in a certain sense, to the effect of increasing stratification for the case of discrete vortices (decrease in the parameter γ)[10]. It is clear that, as in section 3.2, the

[10]This fact was noted in subsection 3.2.2 with respect to the vortex structure having the form of the eccentric roundabout.

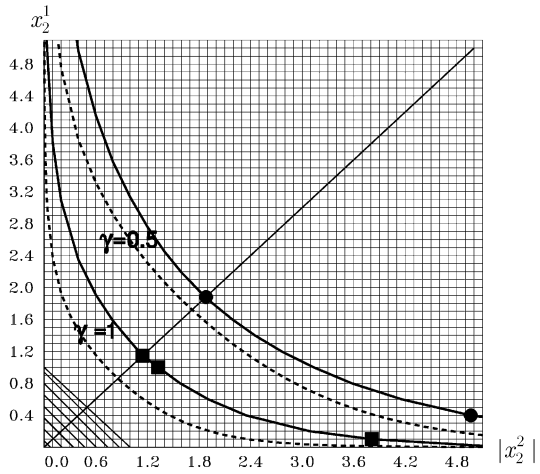

Fig. 25. Dispersion curves in the plane $\left(|x_2^2|;\ x_2^1\right)$ for two different values of the stratification parameter γ for collinear constructions of three discrete (dashed line) and finite-core (solid line) vortices. Marker positions give values of the distance between the centers of the vortex patches in the experiments shown in Fig. 26 and 27.

quantity L_0^{fc} (the finite-core analog of L_0) is not constant. Thus, for example, $L_0^{fc} = 0.942$ at $\gamma = 0.5$ and $L_0^{fc} = 1.146$ at $\gamma = 1$.

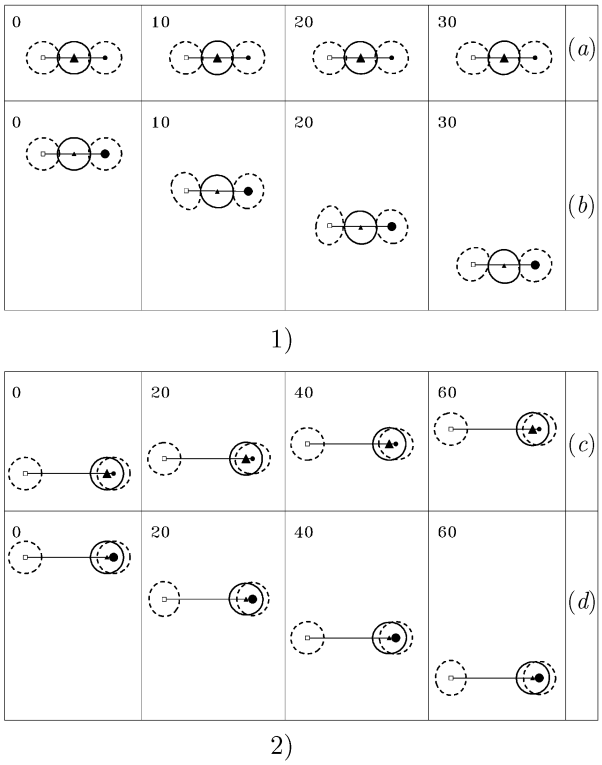

Fig. 26. Synchronous pictures of the vortex-patch contours in the two-layer structures of the triton type at $\gamma = 0.5$ and initial conditions $x_1^1 = 0$ and 1) $-x_2^2 = x_2^1 = 1.883$; 2) $-x_2^2 = 4.962$; $x_2^1 = 0.4$: a) and c) — condition I is fulfilled; b) and d) — condition II is fulfilled. Circular markers in Fig. 25 correspond to geometric conditions of these experiments.

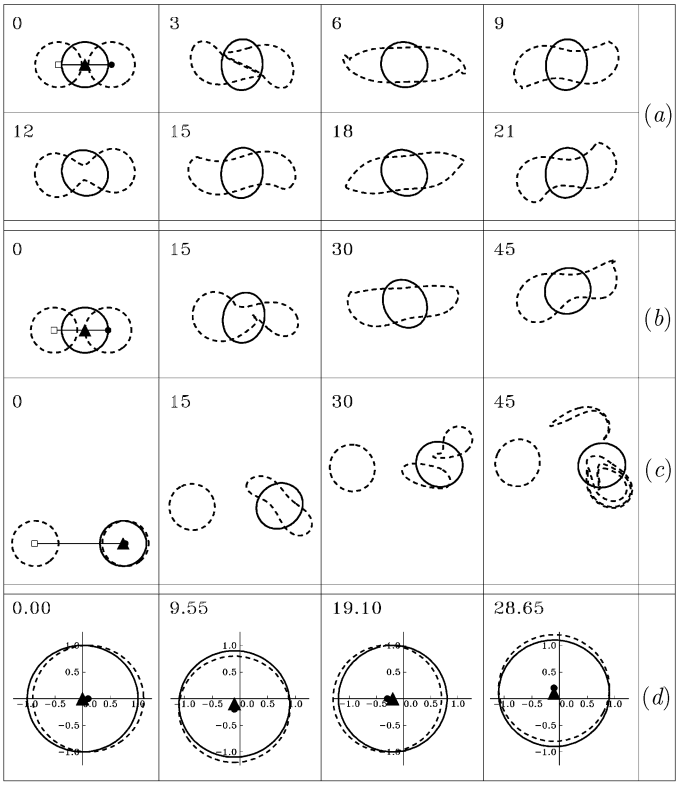

Fig. 27. The lines (a)–(c) — the same as in Fig. 26, but at $\gamma = 1$ and under the fulfillment of condition I: (a) $-x_2^2 = x_2^1 = 1,146$; (b) $-x_2^2 = 1.328$; $x_2^1 = 1$; (c) $-x_2^2 = 3.812$; $x_2^1 = 0.1$. Box markers in Fig. 25 correspond to geometric conditions of these experiments. (d) Evolution of the two-layer structure composed of two vortex patches $\binom{1}{1}$ and $\binom{1}{2}$ when the vortex $\binom{2}{2}$ is absent in the case (c).

Computational results shown in Fig. 26 indicate that if the stratification is sufficiently strong ($\gamma = 0.5$), the shape of the vortex patches during the evolution process does not deflect much from a circular one, and their centers behave qualitatively like discrete vortices composing a triton. In fact, Fig. 26.1 shows, as before, that for $l_0^{fc} = |x_2^2| = x_2^1 = L_0^{fc}/\gamma$ the conditions $V_1 = 0$ and $V_2 < 0$ are fulfilled and, according to Fig. 26.2, $V_1 > 0\,(< 0)$ for $|x_2^2| > x_2^1\,(|x_2^2| < x_2^1)$ and $|V_2| > |V_1|$.

With weaker stratification ($\gamma = 1$), the finite-core vortices behave quite differently. Figure 27 demonstrates three series of computations under condition I for different positions of vortex-patch center dislocation.

When the triton velocity is equal to zero (thus Fig. 27a is an analog of Fig. 26a), the bottom-layer vortices merge. As a result, we have a motionless two-layer structure with zero total intensity, composed of a pulsing quasi-circular anticyclonic vortex in the upper layer and a quasi-elliptic vortex formed after the cyclones have merged in the lower layer. The set of the parameter values $l = |x_2^2| \equiv x_2^1$ and γ, which defines such vortex systems, belongs to the boundary between the areas IMR and ORM in Fig. 2. The cross on the boundary corresponds to the conditions described above.

Figure 27b shows a series of vortex-patch contour configurations, when in the lower layer the vortices also merge but, in view of $|x_2^2| > x_2^1$, the conditions for the vortex system to move in the positive direction of the y-axis are fulfilled. This also explains why the shape of the newly formed lower-layer vortex patch, unlike the previous case, does not possess central symmetry.

The following experiment (Fig. 27c) is carried out for the case where, at the initial instant, the upper layer vortex almost completely covers one of the bottom vortex patches. The stability analysis of the isolated two-layer vortex with vertical axis (the external parameters having analogous values)

shows that the construction must be stable with respect to relatively *small* perturbations in the vortex-patch contour shapes. As shown in [57], a small tilt of the vortex axis does not significantly affect stability. Thus, since the second bottom vortex is absent, the remaining two-layer vortex does not have to split. Figure 27d, illustrating the evolution of such a two-layer vortex, proves this. This line of frames was significantly scaled up; the coordinate axes are drawn to make the figure clearer. The vortices, almost without changing their shape, rotate around their common vorticity center with period of 38.2 dimensionless units. Here, the vortex contours are shown over a quarter of period.

Reverting to Fig. 27c, let us note that the bottom vortex patch $\binom{1}{2}$, being a part of the two-layer construction, breaks up because of *finite* perturbations, induced by the second vortex. Later on, repeated partial merging and mass-exchange occur in the newly formed lower-layer vortex patches. As in Fig. 26c, the vortex system as a whole moves forward along the y-axis.

A comparison of Fig. 26 and Fig. 27 shows that, for finite-core vortices, "pure" tritons, i. e. vortex structures without merging and splitting of vortex patches, may be observed only when $\gamma < 1$ (relatively strong stratification of the fluid or relatively small vortices).

5.3.3. Symmetric triangular configuration — case *I* (discrete vortices)

It is known [4, 27, 66] that in a *homogeneous* fluid a set of three vortices with intensities $(-2\kappa,\ \kappa,\ \kappa)$, organized as an *equilateral triangle* (of arbitrary side length), tends to move uniformly and rectilinearly in the direction parallel to the side facing the strong vortex. The orientation and the velocity of such motion are as those as if there were two vortices for which the vortices of intensities κ were replaced by one vortex with intensity 2κ placed at the midspan of the segment joining both vortices. This configuration is unstable.

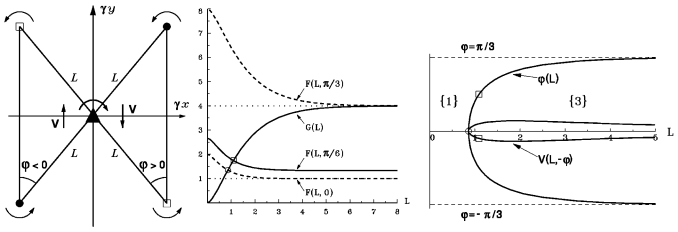

Fig. 28. Characteristics of the triangular vortex construction in the form of an isosceles triangle: (a) Sketch of vortex position; (b) Graphic solution of equation (5.10); (c) Dispersion curve $\phi(L)$, satisfying equation (5.10), and corresponding dependency equation (5.11) for the velocity of the translational movement.

Consider a *two-layer* fluid with conditions I fulfilled and a configuration in the shape of an *isosceles triangle* such that the lower-layer vortices with intensities $\kappa_2^1 = \kappa_2^2 \equiv \kappa$ form its base, and the sides of length l make the angle ϕ with the base. The angle ϕ is measured from the collinear vortex position; its positive value corresponds to the situation when the lower-layer vortices are located in the right part of the figure (the graph in Fig. 28a is referred to the coordinates γx, γy). In this case, for a fixed distribution of the vortex intensity sign, it results in the situation for which $V < 0$ for $\phi > 0$ and $V > 0$ for $\phi < 0$. From the equations (2.1)–(2.2), it is easy to obtain the conditions for the existence of a uniform, rectilinear motion of the vortex structure along the y-axis:

$$F\big(L,\ \phi\big) = G(L), \tag{5.10}$$

where

$$F\big(L,\ \phi\big) = \frac{1 + 2L|\cos\phi| K_1(2L|\cos\phi|)}{\cos^2\phi}, \quad G(L) = 4[1 - LK_1(L)].$$

As before, $L = \gamma l$. Equation (5.10), like equation (5.8), is a dispersion equation, relating the length of the lateral side of the isosceles triangle to the angle at its bottom. It is easy to see that $G(L) \in [0,\ 4)$ and is a monotonously increasing function, whereas $F(L,\ \phi)$ decreases with respect to the first argument and increases when $|\phi|$ grows from 0 to $\pi/3$, given that the conditions $F(L,\ 0) \in [2,\ 1)$ and $F(L,\ \pm\pi/3) \in [8,\ 4)$ are fulfilled. Hence, equation (5.10) possesses a solution (which is unique) only on the interval $|\phi| < \pi/3$. Thus, in the two-layer case the triangle cannot be *equilateral* (more exactly, only in the limit $L \to \infty$, we get $|\phi| = \pi/3$)[11]. Figure 28b demonstrates the behavior of the functions $L(\phi)$ and $V(\phi)$ from (5.10). The limiting positions $F(L,\ \pm\pi/3)$ and $F(L,\ 0)$ are shown as a dashed line. It is clear that the solutions of equation (5.10) correspond to the intersection points of the curves F and G. The position of the circular and box markers in the figure are determined by the coordinates of the intersection points for $\phi = 0$ and $|\phi| = \pi/3$, respectively.

According to (2.1)–(2.2), the expression for the velocity of the appropriate triangular construction in the direction parallel to the base of the triangle is as follows:

$$V = -\frac{\kappa\gamma \sin\phi}{4\pi L}\Big[1 - LK_1(L)\Big]. \tag{5.11}$$

The velocity in this equation, as in the barotropic case, coincides with the velocity of a hypothetical pair composed of vortices with intensities -2κ and 2κ, and separated from each other by a distance equal to the height of the corresponding isosceles triangle. This differs from the barotropic case in that the vortices are located in *different* layers.

Figure 28c demonstrates the behavior of the functions $\phi(L)$ and $V(L, \phi)$, which are solutions of equations (5.10) and (5.11). The meaning of the markers is the same as in Fig. 28b. At $\phi = 0$, the symmetric triangular configuration degenerates into the collinear configuration; in this case, $V = 0$ and L becomes L_0 (see section 3) when the vortex construction is motionless. As shown in the figure, the curve $\phi(L)$ divides the plane $(L,\ \phi)$ into the areas in which motions of types $\{1\}$ and $\{3\}$ take place. Here, each line $L\sin\phi = \text{const}$[12] corresponds to the straight line $t_2 = t_3$ of the corresponding phase portrait.

Figure 29 demonstrates the behavior of a stationary symmetric triangular vortex configuration which, at the initial stage, moves as a whole with velocity (5.11), and then, because of instability, loses this property. In doing so, bottom vortices exchange positions by passing periodically through the collinear state. It is obvious that formula (5.7) is fulfilled in this case. A similar phenomenon occurs in a homogeneous fluid [4]. However, in the two-layer case, such reorganization can take place due to different mechanisms: either the upper-layer anticyclone captures the lower-layer vortices (type $\{3\}$, Fig. 29a), or it occurs because of the predominance of interlayer interaction (type $\{1\}$, Fig. 29b). In both examples, two pairs of instantaneous triangular and collinear configurations were selected. The initial vortex coordinates in both experiments differ insignificantly, and lie in the vicinity of the point on the dispersion curve (Fig. 28c) marked by a white square box. They are (respectively) a little higher and a little lower than this point.

5.3.4. Symmetric triangular configuration (finite-core vortices)

Here, we discuss only two special cases: $\phi = \pi/6$ and $\phi = \pi/4$. It is clear that for discrete vortices, for any fixed value of ϕ (and, consequently, the value of L is also fixed), the $l(\gamma)$ curves consist of hyperbolae $l = L/\gamma$, shown in Fig. 30 as a dashed line on the interval $\gamma \in (0.0;\ 1.0]$; l is the length of the side of the equilateral triangle corresponding to the stationary state. For the finite-core vortices,

[11] In the model of continuously stratified fluid on the β-plane [25], an equilateral triangle corresponding to the stationary solution is plotted in such a way that one of its sides is aligned horizontally and the compensating vortex — in the other level. If we make the relative height of the upper vortex with respect to the two lower vortices equal to the layer thickness, then projecting the triangle onto the horizontal plane and letting β to 0, the dispersion equation (12) from [25] comes into accordance with (5.10) in the present work.

[12] The value of the vortex-system momentum determines the value of the constant.

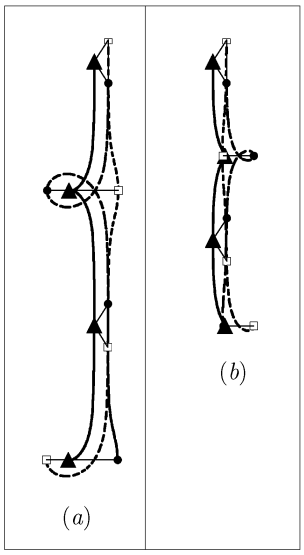

Fig. 29. Evolution of the unstable triangular configuration of the discrete vortices at $\phi = \pi/6$ and (a) $L = 1.092$; (b) $L = 1.084$. The box marker in Figs. 28b, 28c corresponds to the initial condition of the system.

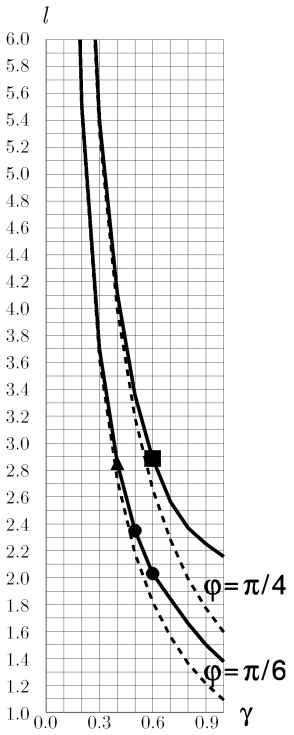

Fig. 30. Dispersion curves in the plane (γ, l) for unstable triangular configurations at $\phi = \pi/6$ and $\phi = \pi/4$ composed of three discrete (dashed line) and three finite-core (solid line) vortices. Coordinates of the triangular and circular markers correspond to the parameters of the numerical experiments given in Figs. 31 and 32.

the $l(\gamma, \phi)$ curves were obtained numerically and are plotted as a solid line. It is obvious that the increase in the angle ϕ has a similar effect as the increase in stratification, i. e. the decrease in γ (analogous curves for $\phi = 0$ are shown in the left part of Fig. 2).

A qualitative comparison of the behavior of the finite-core and discrete vortices is made in Fig. 31. There two series of contour positions for the case $\phi = \pi/6$ are shown. For fixed values ϕ and γ, transition from type $\{3\}$ motion to type $\{1\}$ motion results only from a insignificant decrease in the parameter l. In Fig. 30 one triangular marker covers both corresponding points of the plane (γ, l). However, it should be noted that it is possible to observe such an analogy with the discrete vortices only for relatively small values of the parameter γ (in this case, in particular, $\gamma = 0.4$), when the interaction between the vortices of different layers is weak. As shown by computations, for $\gamma > 0.4$ it is no longer possible to obtain a non-breaking configuration of type $\{1\}$ (as that in Fig. 31b).

The interval for the existence of motions of type $\{3\}$ with respect to the parameter γ is slightly wider[13], as shown by Fig. 32. Figure 32a provides a detailed picture of the evolution of the vortex patches and, in particular, it shows the process of bottom-vortex reconstruction. Figure 32b should be discussed in greater detail. During the first stage, the vortices behave according to the type $\{1\}$ scenario. Later on, the vortex patches in the bottom layer merge and then split into unequal parts (moment of time 16). Further merging was not observed. In this process, a significant quantity of

[13]This is due to the fact that, in the course of the reconstruction of the triangular configuration from one state of a type $\{3\}$ motion, the distance between the vortices in the lower layer happens to be greater than during type $\{1\}$ motions. The trajectories of the discrete vortices in Fig. 29 illustrate this quite well.

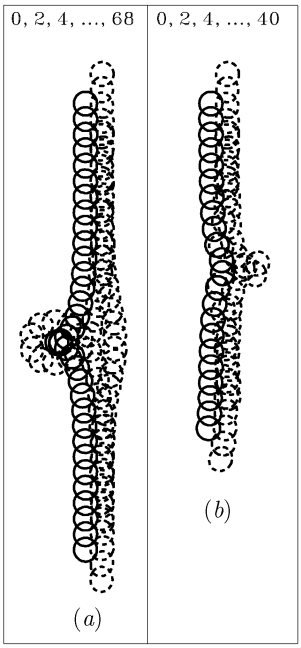

Fig. 31. Positions of the contours of the finite-core vortices representing a stationary triangular configuration in the specified moments of the dimensionless time at $\phi = \pi/6$ and $\gamma = 0.4$: (a) $l = 2.856$; (b) $l = 2.851$. A triangular marker in Fig. 30 corresponds to the conditions of these experiments.

the vorticity (about 22% in this case) is lost because of filamentation. As a result, the influence of the upper vortex becomes stronger and it captures in the anticyclonic motion (that it induces) the configuration formed of the lower-layer big and small vortex patches.

The increase in the angle ϕ to the value $\pi/4$ (the box marker in Fig. 30) slightly stabilizes the situation. The computation (not given here) for the appropriate parameter values, i.e. when $\gamma = 0.6$, gives the configuration analogous to that in Fig. 32a, where $\gamma = 0.4$.

Therefore we can state that, as in the case of the triton vortex (subsection 5.3.2), the theory of point vortices may provide a qualitative description of finite-core vortex behavior only for $\gamma < 1$.

5.3.5. Asymmetric triangular configuration — case *II*

In this concluding section we would like to provide a short analysis of a stationary triangular system when two vortices with opposite signs are located in the bottom layer, one of which is strong.

In case I, the distribution of vortex intensities governs both the symmetry in the stationary triangular configuration, and the direction of its motion, but in case II all the parameters of the corresponding triangle (e.g. lengths of its two sides and the angle between them) and the orientation of the structure with respect to a certain direction must be found.

Let the vortices located in the plane $(\gamma x, \gamma y)$ have the configuration shown in Fig. 33a, where, as assumed earlier, the overall distance of the strong vortex (in this case the lower-layer cyclone) to the other two is $2L$. The requirements of uniform solid-body motion of a triangular construction along the y-axis reduce the problem to the two dispersion equations:

$$\frac{\sin\alpha}{A}\Big[1 - AK_1(A)\Big] - \frac{\sin\beta}{B}\Big[1 + BK_1(B)\Big] - \frac{A\sin\alpha - B\sin\beta}{C^2}\Big[1 - CK_1(C)\Big] = 0, \tag{5.12}$$

$$\frac{\cos\alpha}{A}\Big[1 - AK_1(A)\Big] + \frac{\cos\beta}{B}\Big[1 + BK_1(B)\Big] = 0, \tag{5.13}$$

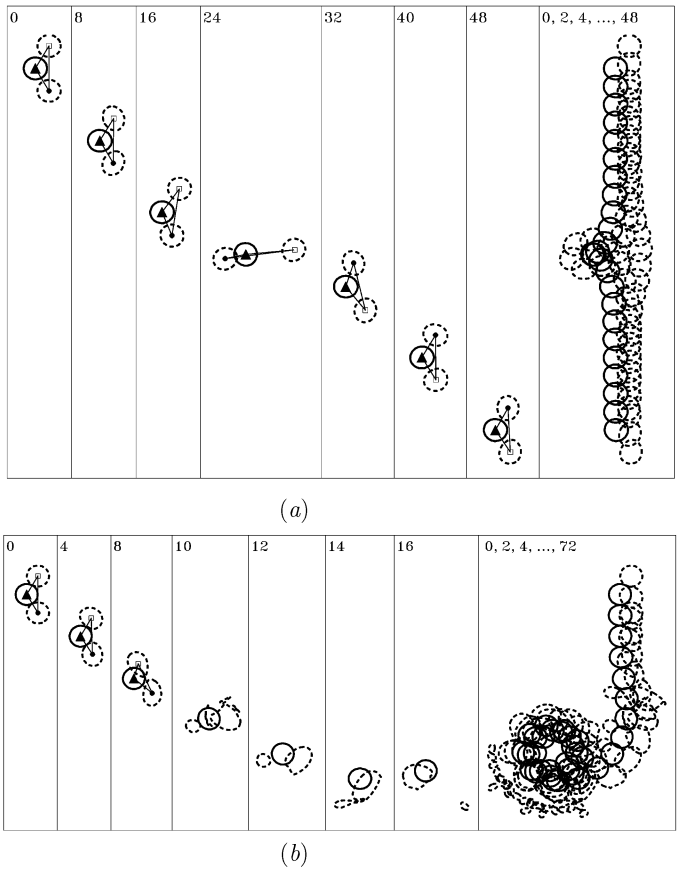

Fig. 32. The same as in Fig. 31 at $\phi = \pi/6$: (a) $\gamma = 0.5$; $l = 2.35$; (b) $\gamma = 0.6$; $l = 2.03$. Circular markers in Fig. 30 correspond to the conditions of these experiments.

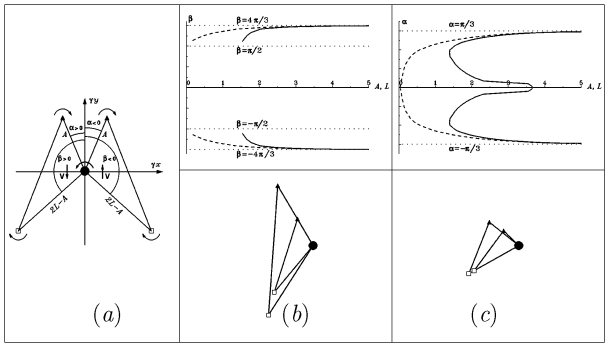

Fig. 33. Characteristics of triangular vortex construction in case II: (a) Scheme of vortex location; (b) $\alpha = \pi/6$: Dispersion curves $L(\beta)$ — solid line and $A(\beta)$ — dashed line as solutions of the equations (5.12)–(5.13) — upper part of the figure; examples of stationary vortex configurations at $\beta = 51^o$ and $\beta = 58^o$ — lower part; (c) $\beta = 2\pi/3$: Dispersion curves $L(\alpha)$ — solid line and $A(\alpha)$ — dashed line — upper part; examples of stationary vortex configurations at $\alpha = 45^o$ and $\alpha = 55^o$ — lower part.

where

$$B = 2L - A, \qquad C = \sqrt{A^2 + (2L - A)^2 - 2A(2L - A)\cos(\beta - \alpha)}.$$

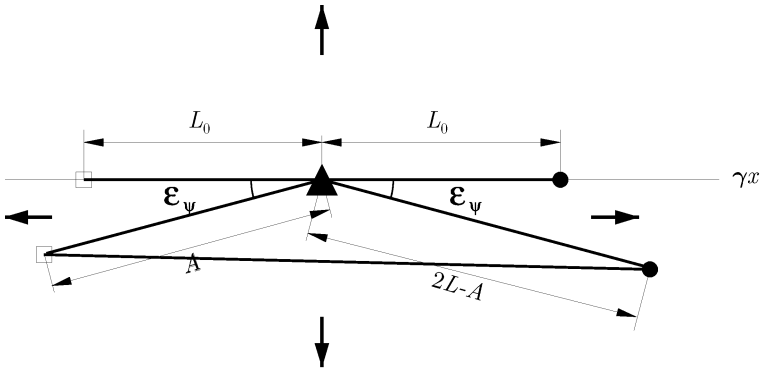

Fig. 34. General scheme of three-vortex location in case I, explaining Table 2. Short arrows have the same meaning as in the table and indicate the direction of motion of the corresponding vortex structures.

Thus, (5.12)–(5.13) establish relations between the parameters A, L, α and β. It is clear that always $A \leqslant L$ and assymptotically $A = L \to \infty$ at $\beta = \pi/2 - \alpha$. Moreover, it follows from (5.13) that the conditions $0 < \alpha < \pi/2$, $\pi/2 < \beta < \pi$ are necessary for the triangular stationary state to exist.

The upper diagrams of Fig. 33b and Fig. 33c illustrate the dispersion curves $A(\beta)$, $L(\beta)$ obtained numerically for a fixed value of α, and $A(\alpha)$, $L(\alpha)$ obtained for a fixed value of β. Examples of the stationary triangular configurations for the given parameter values are shown in the bottom diagrams of the figures.

6. Summary

In this work, the problem of the motion of three vortices in a two-layer rotating fluid with equal layer thicknesses is examined. The total vortex intensity is zero.

Two main assumptions are made about the configuration of the vortex system: 1) two of the three vortices are of equal intensity; 2) one of the vortices belongs to the upper layer, and the other two to the lower layer. Two special cases are discussed in detail, namely I: $(-2;\ 1,\ 1)$ and II: $(-1;\ 2,\ -1)$ where the numbers in parentheses give the values of the upper- and lower-layer vortex intensities, respectively. It should be noted that all the results remain valid if every vortex moves in the other layer. If every vortex changes its sign, all the motions would stay the same except that the rotational sign would be reversed.

Below, some of the main results of this work are summarized:

- A classification is made of the possible types of relative motions of three discrete vortices. It has been shown, that in the general case, the vortex system practically always executes a periodic motion, taking a collinear position at least twice over a period. Qualitatively different types of possible motion are shown to depend on the shape of the initial (collinear) vortex dislocation. The relative interplay of inside-layer effects vs. layer-coupling effects will result in different types of interaction for the vortices, which may be either barotropic, or baroclinic or a mixture of both.
- The conditions under which purely collinear solutions of the equations of motion for three discrete vortices exist are obtained. The following configurations of three discrete vortices were considered:
  - Rotational:
    Ordinary and *Inverse Roundabout* (case I when $P = 0$) — rotation of the peripheral vortices, located in one of the layers, respectively in the same direction as, or opposite direction to, the direction of rotation of the central vortex of the other layer;

Table 2

Parameters	State of the vortex system
$\varepsilon A = \varepsilon L = \varepsilon\psi = 0$	Unstable motionless position
$\varepsilon\psi = 0$: $\varepsilon A < \varepsilon L \leqslant 0$ or $\varepsilon L < \varepsilon A \leqslant 0$	Motions of type $\{1\}\uparrow$ or type $\{1\}\downarrow$, respectively
Particular case: $\varepsilon A = \varepsilon L = \varepsilon < 0$	Inverse Roundabout (IR)
$0 \leqslant \varepsilon A < \varepsilon L$ or $0 \leqslant \varepsilon L < \varepsilon A$ and $\varepsilon\psi = 0$	Motions of type $\{3\}\downarrow$ or type $\{3\}\uparrow$
Particular case: $0 < \varepsilon L = \varepsilon A = \varepsilon$ and $\varepsilon\psi = 0$	Ordinary Roundabout (OR)
$\varepsilon A = \varepsilon L = \varepsilon < 0$, and $\varepsilon\psi > 0$ or $\varepsilon\psi < 0$	Motions of type $\{1\}\leftarrow$ or type$\{1\}\rightarrow$
$\varepsilon A = \varepsilon L = \varepsilon > 0$, and $\varepsilon\psi > 0$ or $\varepsilon\psi < 0$	Motions of type $\{3\}\leftarrow$ or type $\{3\}\rightarrow$
Particular cases: the values $A = L = L_0 + \varepsilon$ and $\cos\phi = \cos\varepsilon\psi$ satisfy equation (5.8) at the same two conditions for $\varepsilon\psi$	Unstable symmetrical triangular configurations $\leftarrow$ or $\rightarrow$
$\varepsilon\psi = 0$: $\varepsilon A > 0$, $\varepsilon L < 0$ or $\varepsilon L > 0$, $\varepsilon A < 0$	Motions of type $\{2\}\downarrow$ or type $\{2\}\uparrow$
Particular cases: the values $A = L_0 + \varepsilon A$ and $L = L_0 + \varepsilon L$ satisfy equation (5.10) at the same two conditions for εA and εL	Tritons $\downarrow$ or $\uparrow$

Eccentric Roundabout (case II when $P = 0$) — rotation of the vortices around their vorticity center in the direction induced by the stronger vortex. As this takes place, the strong vortex occupies a certain intermediate position in the segment linking all the three vortices. The vorticity center is located between it and the vortex of the other layer.

– Translational:

Triton (cases I and II when $P \neq 0$ and the dispersion equalities (28) are fulfilled) — uniform rectilinear motion of the two-layer three-vortex Λ-shaped structure.

- We have found a class of unstable solutions that is characterized by a uniform translational motion of the *triangular construction* for $P \neq 0$. This construction has the form of an isosceles triangle (case I) and a scalene triangle (case II).
- The analysis is also made of some specific properties of vortices respect to whether they are discrete or distributed ones. Noticeable differences are observed and tentatively explained. Note that the numerical experiments are realized using the two-layer version of the CDM.

In conclusion, let us return to the case I, when the vortex construction is Λ-shaped (the upper-layer vortex is in an intermediate position between peripheral partners of the lower layer). Such three-vortex configurations are shown in Fig. 34.

Let us examine, in the space of variables (A, L, ψ), point $\Omega = (L_0, L_0, 0)$ and its vicinity where $A = L_0 + \varepsilon_A$, $L = L_0 + \varepsilon_L$, $\psi = \varepsilon_\psi$. The conditions $|\varepsilon_A|$, $|\varepsilon_L|$, $|\sin\varepsilon_\psi| << 1$ are supposed. The states of the vortex system are characterized in Table 2; arrows point to the direction of motion of the corresponding construction vorticity center, shown in Fig. 34. The table clearly shows the bifurcation characteristic of the point Ω.

Without delving into the analysis of case II, let us note that in this case the configuration of three vortices, corresponding to the point Ω (and *only* to this point), determines the *unstable* triton state, branching into the solutions of types $\{1\}$ and $\{2b\}$.

Acknowledgment

At different stages of the preparation of this work, the results were discussed with V. M. Gryanik, V. V. Kozlov, A. V. Borisov, O. I. Yakovenko, J. B. Flór, X. J. Carton, V. N. Zyryanov, Z. I. Kizner, G. M. Reznik, V. V. Zhmur, A. N. Vulfson, S. K. Gulev, T. R. Kilmatov. The authors are very grateful to them for their assistance. The work of MAS was carried out thanks to the financial support of the Russian Foundation for Basic Research (Project 01-05-64646) and the French National Center for Scientific Research (CNRS).

References

[1] *H. Aref.* Motion of Three Vortices. Phys. Fluids. 1979. V. 22. №3. P. 393–400.

[2] *H. Aref.* Point Vortex Motion With a Center of Symmetry. Phys. Fluids. 1982. V. 25. №12. P. 2183–2187.

[3] *H. Aref.* The Numerical Experiment in Fluid Mechanics. J. Fluid Mech. 1986. V. 173. P. 15–41.

[4] *H. Aref.* Three-Vortex Motion With Zero Total Circulation: Addendum. J. Appl. Math. Phys. (ZAMP) 1989. V. 40. P. 495–500.

[5] *H. Aref, J. B. Kadtke, I. Zawadski, L. J. Campbell, B. Eckhardt.* Point Vortex Dynamics: Recent Results and Open Problems. Fluid Dyn. Res. 1988. V. 3. P. 63–74.

[6] *H. Aref, M. A. Stremler.* On the Motion of the Three Point Vortices in a Periodic Strip. J. Fluid Mech. 1996. V. 314. P. 1–25.

[7] *H. Aref, M. A. Stremler.* Four-Vortex Motion With Zero Total Circulation and Impulse. Phys. Fluids. 1999. V. 11. №12. P. 3704–3715.

[8] *V. I. Arnold, V. V. Kozlov, A. I. Neishtadt.* Mathematical Aspects of Classical and Celestal Mechanics. Actual Problems of Mathematics. Fundamental Tendency. (Results in Science and Technics), Moscow, VINITI AS USSR. 1985. V. 3. P. 304. (In Russian)

[9] *J.-M. Baey, X. Carton.* Vortex Multipoles in Two-Layer Rotating Shallow-Water Flows. J. Fluid Mech. 2002. V. 460. P. 151–175.

[10] *E. S. Benilov, D. Broutman, E. P. Kuznetsova.* On the Stability of Large-Amplitude Vortices in a Continuously Stratified Fluid on the f-Plane. J. Fluid Mech. 1998. V. 355. P. 139–162.

[11] *A. V. Borisov, I. S. Mamaev.* Poisson Structures and Lie Algebras in Hamiltonian Mechanics. Izhevsk: RCD. 1999. P. 464. (In Russian)

[12] *G. F. Carnevale, R. C. Kloosterziel.* Emergence and Evolution of Triangular Vortices. J. Fluid Mech. 1994. V. 259. P. 305–331.

[13] *X. J. Carton, S. M. Correard.* Baroclinic Tripolar Vortices: Formation and Subsequent Evolution. In: Sorensen, Hopfinger and Aubry (eds), Simulation and Identification of Organized Structures in Flows. IUTAM/SIMFLOW Simp. Kluwer Acad. Publ. 1999. V. 52. P. 181–190.

[14] *X. J. Carton, G. R. Flierl, L. M. Polvani.* The Generation of Tripoles from Unstable Axisymmetric Isolated Vortex Structures. Europhys. Lett. 1989. V. 9. №4. P. 339–344.

[15] *X. Carton, B. Legras.* The Life-Cycle of Tripoles in Two-Dimensional Incompressible Flows. J. Fluid Mech. 1994. V. 267. P. 53–82.

[16] *S.-Y. Chao, P.-T. Shaw.* Close Interactions Between Two Pairs of Heton-Like Vortices Under Sea Ice. J. Geophys. Res. 1999. V. 104. №C10. P. 591–605.

[17] *J. P. Christiansen, N. J. Zabusky.* Instability, Coalescence and Fission of Finite-Area Vortex Structures. J. Fluid Mech. 1973. V. 31. P. 219–243.

[18] *S. M. Correard, X. J. Carton.* Vertical Alignment of Geostrophic Vortices: On the Influence of the Initial Distribution of Potential Vorticity. In: Sorensen, Hopfinger and Aubry (eds.), Simulation and Identification of Organized Structures in Flows. IUTAM/SIMFLOW Simp. Kluwer Acad. Publ. 1999. V. 52. P. 191–200.

[19] *S. M. Correard, X. J. Carton.* Formation and Stability of Tripolar Vortices in Stratified Geostrophic Flows. Il Nuovo Cimento. 1999. C 22. №6. P. 767–777.

[20] *B. Eckhardt.* Integrable Four Vortex Motion. Phys. Fluids. 1988. V. 31. №10. P. 2796–2801.

[21] *G. R. Flierl, V. D. Larichev, J. C. McWilliams, G. M. Reznik.* The Dynamics of Baroclinic and Barotropic Solitary Eddies. Dyn. Atmos. Oceans. 1980. V. 5. P. 1–41.

[22] *J. B. Flor, W. S. S. Govers, G. J. F. van Heijst, R. van Sluis.* Formation of a Tripolar Vortex in a Stratified Fluid. Appl. Sci. Res. 1993. V. 51. №1–2. P. 405–409.

[23] *V. M. Gryanik.* Dynamics of Singular Geostrophic Vortices in a Two-Layer Model of Atmosphere (Ocean). Izvestia, Atmos. Oceanic Phys. 1983. V. 19. №3. P. 227–240. (In Russian) P. 171–179. (English translation)

[24] *V. M. Gryanik.* Singular Geostrophic Vortices on the β-Plane as a Model for Synoptic Vortices. Oceanology. 1986. V. 26. №2. P. 174–179. (In Russian) P. 126–130. (English translation)

[25] *V. M. Gryanik.* Localized Vortices — 'Vortex Charges' and 'Vortex Filaments' in a Baroclinic Differentially Rotating Fluid. Izvestia, Atmos. Oceanic Phys. 1988. V. 24. №12. P. 1251–1261. (In Russian) P. 919–926. (English translation)

[26] *V. M. Gryanik.* About Theoretical Models of the Localized Quasi-Geostrophic Eddies in the Atmosphere and Ocean. In: The Investigations of Vortex Dynamics and Energetics of the Atmosphere, and Problems of Climate (Ed. E. G. Nikiforov and V. F. Romanov). Leningrad, Gidrometeoizdat. 1990. P. 31–60. (In Russian)

[27] *G. J. F. van Heijst.* Topography Effects on Vortices in a Rotating Fluid. Meccanica. 1994. V. 29. №4. P. 431–451.

[28] *G. J. F. van Heijst, R. C. Kloosterziel.* Tripolar Vortices in a Rotating Fluid. Nature. 1989. V. 338. №6216. P. 569–571.

[29] *G. J. F. van Heijst, R. C. Kloosterziel, C. W. M. Williams.* Laboratory Experiments on the Tripolar Vortex in a Rotating Fluid. J. Fluid Mech. 1991. V. 225. P. 301–331.

[30] *J. S. Hesthaven, J. P. Lynov, J. J. Rasmussen, G. G. Sutyrin.* Generation of Tripolar Vortical Structures on the Beta Plane. Phys. Fluids. 1993, A 5. №7. P. 1674–1678.

[31] *N. G. Hogg, H. M. Stommel.* The Heton, an Elementary Interaction Between Discrete Baroclinic Geostrophic Vortices, and its Implications Concerning Eddy Heat-Flow. Proc. Roy. Soc. London. 1985. A. 397. P. 1–20.

[32] *E. J. Hopfinger, G. J. F. van Heijst.* Vortices in Rotating Fluids. Ann. Rev. Fluid Mech. 1993. V. 25. P. 241–289.

[33] *M. Ikeda.* Instability and Splitting of Mesoscale Rings Using a Two-Layer Quasi-Geostrophic Model on a f-Plane. J. Phys. Oceanogr. 1981. V. 11. №7. P. 987–998.

[34] *T. P. Konovalyuk.* Classification of Interactions of a Vortex Pair With a Point Vortex in an Ideal Fluid. Fluid Mechanics. 1990. V. 62. P. 64–71. (In Russian)

[35] *V. F. Kozlov, V. G. Makarov, M. A. Sokolovskiy.* Numerical Model of the Baroclinic Instability of Axially Symmetric Eddies in Two-Layer Ocean. Izvestia, Atmos. Oceanic Phys. 1986. V. 22. №8. P. 868–874. (In Russian) P. 674–678. (English translation)

[36] *V. V. Kozlov.* General Theory of the Vortices. Izhevsk: RCD. 1998. P. 240. (In Russian)

[37] *V. D. Larichev, G. M. Reznik.* On Collision Between Two-Dimensional Solitary Rossby Waves. Oceanology. 1983. V. 23. №5. P. 725–734. (In Russian) P. 545–552. (English translation)

[38] *B. Legras, P. Santangelo, R. Benzi.* High-Resolution Numerical Experiments for Forced Two-Dimensional Turbulence. Europhys. Lett. 1988. V. 5. №1. P. 37–42.

[39] *C. E. Leith.* Minimum Enstrophy Vortices. Phys. Fluids. 1984. V. 27. №6. P. 1388–1395.

[40] *V. G. Makarov.* Numerical Simulation of the Formation of Tripolar Vortices by the Method of Contour Dynamics. Izvestia, Atmos. Oceanic Phys. 1996. V. 32. №1. P. 46–55. (In Russian)

[41] *J. S. Marshall.* Chaotic Oscillations and Breakup of Quasigeostrophic Vortices in a N-Layer Approximation. Phys. Fluids. 1995. V. 7. №5. P. 983–992.

[42] *V. V. Meleshko, G. J. F. van Heijst.* Interaction Two-Dimensional Vortex Structures: Point Vortices, Contour Kinematics and Stirring Properties. Chaos, Solitons & Fractals. 1994. V. 4. №6. P. 977–1010.

[43] *V. V. Meleshko, T. P. Konovalyuk.* Interactions of a Vortex Pair With a Point Vortex in a Boundless Ideal Fluid. journalAcad. Nauk Ukrainy. Doklady, Ser. A 1988. №7. P. 43–47. (In Russian)

[44] *V. V. Meleshko, M. Yu. Konstantinov.* Collision of Two Collinear Point Vortices in a Boundless Ideal Fluid. Ukraine Acad. Nauk. Doklady, Ser. A. 1988. №4. P. 33–37. (In Russian)

[45] *V. V. Meleshko, M. Yu. Konstantinov.* Dynamics of Vortex Structures. Naukova Dumka, Kiev. 1993. P. 280. (In Russian)

[46] *Y. G. Morel, X. J. Carton.* Multipolar Vortices in Two-Dimensional Incompressible Flows. J. Fluid Mech. 1994. V. 267. P. 23–51.

[47] *E. A. Novikov.* Dynamics and Statistics of a Vortex System. Sov. Phys. J. Exp. Theor. Phys. 1975. V. 68. №5. P. 1868–1882. (In Russian) V. 41. P. 937–943. (English translation)

[48] *E. A. Novikov, Yu. B. Sedov.* Stochastic Properties of a Four-Vortex System. Sov. Phys. J. Exp. Theor. Phys. 1978. V. 75. №3(9). P. 868–876. (In Russian)

[49] *P. Orlandi, G. J. F. van Heijst.* Numerical Simulation of Tripolar Vortices in 2D Flow. Fluid Dyn. Res. 1992. V. 9. P. 179–206.

[50] *H. Poincaré.* Theorié des Tourbillons. Paris, Georges Carré. 1893. P. 205.

[51] *L. M. Polvani, X. J. Carton.* The Tripole: A New Coherent Vortex Structure of Incompressible Two-Dimensional Flows. Geophys. Astrophys. Fluid Dyn. 1990. V. 51. P. 87–102.

[52] *G. M. Reznik.* Point Vortices on a β-Plane and Rossby Solitary Waves. Oceanology. 1986. V. 26. №2. P. 165–173. (In Russian)

[53] *L. F. Rossi, J. F. Lingevitch, A. J. Bernoff.* Quasi-Steady Monopole and Tripole Attractors for Relaxing Vortices. Phys. Fluids. 1997. V. 9. №8. P. 2329–2338.

[54] *N. Rott.* Three-Vortex Motion With Zero Total Circulation. J. Appl. Math. Phys. (ZAMP). 1989. V. 40. P. 473–494.

[55] *N. Rott.* Constrained Three- and Four-Vortex Problems. Phys. Fluids. 1990, A 2. №8. P. 1477–1480.

[56] *E. N. Selivanova.* Topology of the Three-Vortex Problem. Trudy MI RAN. 1994. V. 205. P. 141–149. (In Russian)

[57] *M. A. Sokolovskiy.* Head-On Collisions of Distributed Hetons. Acad. Nauk SSSR. Doklady. 1989. V. 306. P. 198–202. (In Russian) P. 215–217. (English translation)

[58] *M. A. Sokolovskiy.* Numerical Modelling of the Interaction of Distributed Hetons During Their Head-On Collisions. In: Method of Countor Dynamics in Oceanological Investigations (Ed. V. F. Kozlov). Vladivostok, FED USSR Acad. Sci. 1990. P. 40–57. (In Russian)

[59] *M. A. Sokolovskiy, J. Verron.* Finite-Core Hetons: Stability and Interactions. J. Fluid Mech. 2000. V. 423. P. 127–154.

[60] *M. A. Sokolovskiy, J. Verron.* Four-Vortex Motion in the Two Layer Approximation: Integrable case. Reg. & Chaot. Dyn. 2000. V. 5. №4. P. 413–436.

[61] *M. A. Sokolovskiy, J. Verron.* New Stationary Solutions to the Problem of Three Vortices in a Two-Layer Fluid. Russian Acad. Nauk. Doklady. 2002. V. 383. №1. P. 61–66. (In Russian) Doklady Physics. 2002. V. 47. №3. P. 233–237. (English translation)

[62] *M. A. Sokolovskiy, J. Verron, I. M. Vagina.* Effect of Submerged Small-Height Obstacle on the Dynamics of a Distributed Heton. Izvestia, Atmos. Oceanic Phys. 2001. V. 37. №1. P. 131–143. (In Russian) P. 122–133. (English translation)

[63] *M. Swenson.* Instability of Equivalent-Barotropic Riders. J. Phys. Oceanogr. 1987. V. 17. №4. P. 492–506.

[64] *J. L. Synge.* On the Motion of Three Vortices. Can. J. Math. 1949. V. 1. №3. P. 257–270.

[65] *J. Tavantzis, L. Ting.* The Dynamics of Three Vortices Revisited. Phys. Fluids. 1988. V. 31. №6. P. 1392–1409.

[66] *S. Valcke, J. Verron.* On Interactions Between Two Finite-Core Hetons. Phys. Fluids. 1993, A 5. №8. P. 2058–2060.

[67] *O. U. Velasco Fuentes, G. J. F. van Heijst, N. P. M. van Lipzing.* Unsteady Behaviour of a Topography-Modulated Tripole. J. Fluid Mech. 1996. V. 307. P. 11–41.

[68] *W. R. Young.* Some Interaction Between Small Numbers of Baroclinic, Geostrophic Vortices. Geophys. Astrophys. Fluid Dyn. 1985. V. 33. №1. P. 35–61.

[69] *S. I. Ziglin.* Nonintegrability of the Problem on the Motion of Four Point Vortices. Acad. Nauk SSSR. Doklady. 1980. V. 250. №6. P. 1296–1300. (In Russian)